scientific reports

Check for updates

OPEN

Exploring optoelectronic and photovoltaic properties of Be_3MF_3 (M = P, As, Sb) perovskites via machine learning and numerical simulation

Indrojit Paul[1], Asadul Islam Shimul[1], Bipul Chandra Biswas[1], Karim Kriaa[2], Mohamed Benghanem[3], Md. Azizur Rahman[4], Mekuria Tsegaye Alemu[5]✉ & Noureddine Elboughdiri[6]

This study presents a comprehensive Density Functional Theory (DFT) analysis of the structural, mechanical, electrical, and optical characteristics of cubic Be_3MF_3 (M = P, As, Sb) perovskites, highlighting its potential for optoelectronic applications. The computed elastic constants adhere to the Born stability criterion, affirming mechanical resilience and ductility. Analyses of band structure and density of states reveal that all Be_3MF_3 compounds exhibit indirect band gaps between 2.0 and 3.3 eV, categorizing them as wide-bandgap semiconductors suitable for high-power and UV optoelectronic applications. Optical investigations demonstrate significant absorption, especially in Be_3SbF_3, highlighting its promise as a lead-free absorbing material for solar cell applications. Device-level performance was modeled utilizing SCAPS-1D, incorporating Be_3SbF_3 as the absorber across diverse configurations with four electron transport layers (In_2S_3, TiO_2, Mg:ZnO, IGZO) and six-hole transport layers (Cu_2O, MoO_3, P3HT, NiO, PTAA, V_2O_5). The best configuration, Al/FTO/In_2S_3/Be_3SbF_3/Cu_2O/Ni, attained a maximum power conversion efficiency (PCE) of 18.28%, with open-circuit voltage (V_{OC}) of 1.79 V, short-circuit current (J_{SC}) of 11.04 mA/cm^2, and a fill factor (FF) of 89.6%. Subsequent examinations of defect density, interface states, thickness variation, and temperature impacts clarify charge transport and recombination kinetics. A Random Forest machine learning (ML) model was created to forecast device performance, with high accuracy (R^2 = 0.987, MSE = 0.00305, MAPE = 0.075) and pinpointing bandgap energy and interface defect density as critical limiting factors. The integrated DFT-SCAPS 1D-ML framework identifies Be_3SbF_3 perovskites as viable, lead-free materials for advanced photovoltaic and optoelectronic technologies.

Keywords Be_3MF_3 (M = P, As, Sb), Be_3SbF_3, Optoelectronic and mechanical properties, SCAPS-1D solar cell simulation, Machine learning optimization

Addressing pollution, climate change, and energy insecurity requires a thorough shift to renewable energy systems, especially solar, wind, and hydropower resources. Developing countries receive sun energy much exceeding the world's total coal reserves and current global consumption, highlighting solar power's unparalleled potential[1,2]. As a result, photovoltaic (PV) technologies have emerged as a central focus of research and industry advancement. Recent advancements in perovskite-based solar cells have intensified this trend owing to their exceptional efficiency, cost-effectiveness, and adjustable material characteristics[3,4]. Perovskite solar cells (PSCs) are chiefly classified into A_3BX_3 and ABX_3 structural kinds, each providing distinct advantages

[1]Department of Electrical and Electronic Engineering, Gopalganj Science and Technology University, Gopalganj 8105, Bangladesh. [2]College of Engineering, Imam Mohammad Ibn Saud Islamic University (IMSIU), Riyadh 11432, Saudi Arabia. [3]Physics Department, Faculty of Science, Islamic University of Madinah, Madinah 42351, Saudi Arabia. [4]Department of Electrical and Electronic Engineering, Begum Rokeya University, Rangpur 5400, Bangladesh. [5]Department of Physics, College of Natural and Computational Science, Kebri Dehar University, P.O. Box 250, Kebri Dehar, Ethiopia. [6]Chemical Engineering Department, College of Engineering, University of Ha'il, P.O. Box 2440, 81441 Ha'il, Saudi Arabia. ✉email: mekuria.tsegaye20@uok.edu.et

regarding efficiency, stability, and scalability[5]. The ABX_3 structure, consisting of metal cations (A, B) and halogen anions (X), is the most extensively researched and forms the basis of most metal halide perovskites[6]. Despite significant advancements improving PSC performance, cubic inorganic perovskites continue to encounter issues like moisture sensitivity, structural instability, and scalability in manufacturing. Organic perovskites have excellent efficiency but suffer from inadequate stability, whereas lead-based compounds encounter toxicity and deterioration when exposed to humidity, heat, and ultraviolet radiation[7,8]. Conversely, materials such as carbon nanotubes (CNTs), graphene, and transition metal dichalcogenides (TMDs) have enhanced stability, flexibility, and conductivity, rendering them optimal for hybrid solar designs[9,10]. Carbon nanotubes improve carrier mobility, moisture resistance, and interface quality when combined with perovskites, hence enhancing long-term stability. However, CNT-based devices frequently necessitate intricate surface modifications to attain good band alignment with the absorber layer. Furthermore, bilayer or multi-junction solar cells that incorporate materials with complementary band gaps enhance light absorption and improve power conversion efficiencies; yet, their production necessitates precise lattice and energy-level alignment, frequently resulting in interfacial instability[11].

Researchers are investigating lead-free alternatives that utilize non-toxic cations, demonstrating enhanced chemical stability, tunable bandgaps, and extensive optoelectronic applications to surmount these challenges. Parmar et al.[12] investigated $RbGeX_3$ (X = I, Br, Cl) perovskites by DFT, demonstrating significant structural stability, direct bandgaps, and remarkable optical and thermoelectric properties, with anticipated efficiencies of 15.67%, 22.08%, and 28.93%, respectively. Rehman et al.[13] examined $CsSnX_3$ (X = I, Br, Cl) perovskites using DFT-CASTEP (GGA-PBE), validating their narrow bandgaps, elevated absorption coefficients, and malleable characteristics, hence identifying $CsSnI_3$ as a notably effective contender for solar and LED applications. Zhang et al.[14] examined $InXY_3$ (X = Ca, Sr, Ba; Y = Cl, Br) perovskites, revealing their mechanical strength, extensive bandgaps, and significant UV absorption coupled with visible–infrared transparency, making them suitable for transparent and UV-protective optoelectronic devices.

Inorganic compounds are pivotal to advancements in solar technology because of their distinctive physical and electrical characteristics. Recent research emphasizes materials characterized by the generic formula A_3BX_3, when A represents a large inorganic cation, B denotes a smaller metal cation, and X signifies a halogen anion[15]. Compounds like Mg_3SbF_3, Ba_3PF_3, and Sr_3AsBr_3 exhibit significant thermodynamic stability, ideal bandgaps, elevated absorption coefficients, and anticipated power conversion efficiencies (PCEs) over 25%, making them very interesting candidates for advanced solar cells[16,17,18]. Harun-Or-Rashid et al.[19] investigated Pb-free cubic A_3SbI_3 (A = Ba, Sr, Ca) perovskites by first-principles DFT and SCAPS-1D simulations, validating their mechanical and optical stability. Through the optimization of layer thickness, doping, and flaws, Ba_3SbI_3 attained an exceptional power conversion efficiency (PCE) of 30.26%, surpassing previous versions. Hossain et al.[20] investigated A_3BF_3 (A = Mg, Ca, Sr, Ba; B = N, Bi) perovskites, identifying cubic symmetry, mechanical stability, and significant visible-light absorption. Mg-based compounds functioned as insulators, but Ca-, Sr-, and Ba-based complexes exhibited semiconducting properties appropriate for solar, thermal, and optoelectronic applications. Ghosh et al.[21] conducted an in-depth analysis of A_3BX_3 (A = Ca, Sr; B = P, As; X = I, Br) halide perovskites, documenting direct bandgaps ranging from 1.26 to 2.63 eV, substantial absorption, and elevated efficiency, with Sr_3AsI_3 attaining a PCE of 28.16%. Phosphorus (P), Arsenic (As), and Antimony (Sb) are crucial to improving perovskite efficacy. P serves as a bandgap-tuning dopant, enhancing light absorption and charge mobility; As alters the band structure and prolongs carrier lifetimes; and Sb substitutes hazardous lead, thereby enhancing stability and environmental compatibility[22,23,24]. Collectively, these components provide efficient, lead-free, and resilient perovskite configurations. Nonetheless, synthesis difficulties remain due to the volatility of halogens particularly fluorine (F) and the necessity for meticulous control of stoichiometry, phase purity, and oxidation states, especially in antimony-based systems[25]. Notwithstanding these challenges, ongoing enhancement of synthesis procedures and sophisticated modeling approaches, including GW-BSE simulations to evaluate exciton binding energy[26], are anticipated to expedite the advancement of these materials for next-generation optoelectronic and solar applications.

This study extensively investigated the structural, mechanical, optical, and electrical properties of Be_3MF_3 (M = P, As, Sb) halide perovskites by first-principles DFT calculations to evaluate their suitability for PV applications. Among the candidates, Be_3SbF_3 demonstrated the most advantageous bandgap, stability, and light absorption properties, establishing it as a formidable prospect for solar energy conversion. The SCAPS-1D simulation tool was utilized to assess the PV performance of Be_3SbF_3-based PSCs. An analysis was conducted on various hole transport layers (HTLs) such as Cu_2O, MoO_3, P3HT, NiO, PTAA, and V_2O_5 and electron transport layers (ETLs) including In_2S_3, TiO_2, Mg:ZnO, and IGZO to determine the best device configuration. The impact of absorber thickness, doping concentration, and defect density on the principal PV parameters was methodically investigated. Furthermore, Nyquist plots, J-V characteristics, and quantum efficiency (QE) investigations were performed to investigate charge transport, recombination, and overall device efficiency. Temperature-dependent performance evaluations validated the material's thermal stability. A Random Forest (RF) machine learning model was created to forecast the photovoltaic performance of Be_3SbF_3-based solar cells utilizing an extensive dataset of 13,113 data points obtained from device simulations. The model underwent training and evaluation utilizing several interpretative techniques, such as correlation heatmaps, SHAP (Shapley Additive Explanations) importance analysis, parity plots, and confusion matrix assessments, guarantee thorough feature evaluation and predictive reliability. The RF model exhibited significant predictive accuracy, successfully identifying bandgap energy and interface defect density as the primary factors influencing device efficiency. The combined use of DFT-derived material descriptors, SCAPS-1D device simulations, and ML-based predictions creates a cohesive framework for elucidating performance-limiting mechanisms and progressing Be_3SbF_3 perovskite solar cells towards scalable, lead-free, and sustainable photovoltaic applications.

Computational methodology

A Density Functional Theory (DFT)-based technique was employed inside the Cambridge Serial Total Energy Package (CASTEP) framework to examine the structural, electrical, and optical properties of Be_3MF_3 (M = P, As, Sb) perovskite material. The Generalized Gradient Approximation (GGA) utilizing the Perdew–Burke–Ernzerhof (PBE) functional was utilized to address the exchange–correlation potential and assess the electronic band structure[27]. The Vanderbilt-type ultrasoft pseudopotential On–The–Fly–Generated (OTFG) was employed to precisely simulate the interaction between valence electrons and ionic cores, ensuring computational efficiency and accuracy in total energy calculations[28]. The Broyden–Fletcher–Goldfarb–Shanno (BFGS) minimization technique was employed to optimize the crystal shape, allowing the system to achieve its minimum energy configuration[29]. The Brillouin zone was sampled with a Monkhorst–Pack k-point grid of $10 \times 10 \times 10$, and a plane-wave cutoff energy of 450 eV was utilized. This selection was established by rigorous convergence testing, which verified that these parameters provide very accurate assessments of the structural, electrical, and optical properties without incurring excessive computational costs. The selected k-point density effectively encapsulates the fundamental electronic interactions stemming from the inherent symmetry of the crystal lattice, guaranteeing numerical accuracy in the calculation of mechanical properties, including the elastic constants. The alignment of these computational settings with previously reported[21] further validates their reliability and appropriateness for attaining a balanced trade-off between accuracy and computational efficiency. The elastic properties were ascertained utilizing the finite strain–stress methodology, as executed in CASTEP, to compute the elastic stiffness constants (C_{ij}) under equilibrium conditions[30]. Geometry optimization adhered to rigorous convergence criteria: a maximum displacement of 5×10^{-4} Å, a maximum force of 0.01 eV/Å, a maximum stress of 0.05 GPa, and a total energy convergence of 1×10^{-5} eV per atom. A strain magnitude of 0.003 was utilized in the elastic calculations, guaranteeing computational stability and alignment with previous theoretical studies. These criteria combined guaranteed the dependability and reproducibility of the results obtained. Additionally, to augment the first-principles findings, the SCAPS-1D software was utilized to model charge carrier transit, electrostatic potential distribution, and overall device performance under steady-state conditions[31,32]. The model quantitatively resolved Poisson's and continuity equations for electrons and holes, yielding a comprehensive insight into recombination kinetics, carrier diffusion, and drift phenomena[33,34]. This hybrid computational method integrating quantum–mechanical DFT insights with numerical device modeling facilitated a thorough evaluation of the Be_3SbF_3-based PSC, providing essential guidance for enhancing its optoelectronic characteristics and operational efficiency in advanced PV applications.

Result and discussion

DFT result

Structural properties

The beryllium-based single halide perovskite compounds, represented as Be_3MF_3 (where M = P, As, Sb), crystallize in a cubic A_3BX_3-type perovskite structure that corresponds to the Pm-3 m crystallographic space group (No. 221)[35]. Figure 1a, b illustrates the optimal crystal structure of the Be_3MF_3 systems, showcasing a well-ordered cubic layout including a single formula unit per cell, consisting of seven atoms. The optimized lattice parameters and associated unit cell volumes, derived from GGA-PBE functional, are presented in Table 1. In these structures, the Be atoms predominantly occupy the 3a Wyckoff positions (1/2, 1/2, 0), whereas the M-site elements (P, As, Sb) are located at the 1b Wyckoff locations (1/2, 1/2, 1/2), and the F atoms are situated at the 3c Wyckoff sites (1/2, 0, 0). A comprehensive geometry optimization was conducted, permitting the total relaxation of lattice parameters to achieve the equilibrium configuration. The derived lattice constants and total energy values exhibit remarkable concordance with existing theoretical and experimental findings, hence affirming the

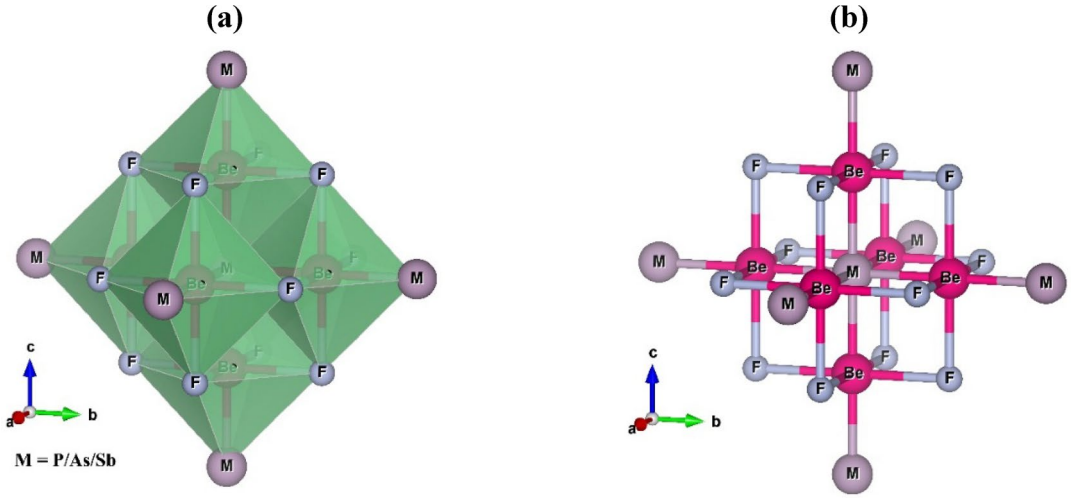

Fig. 1. Graphic representation of Be_3NX_3 compounds: (**a**) polyhedral view, (**b**) ball-and-stick model, for Be_3MF_3.

Material name	Band gap (E_g)	Lattice constant (Å)	Unit cell volume (Å^3)	τ_G	E_f (eV/atom)	Refs.
Be_3PF_3	3.327	4.187	73.409	0.94	−3.98	This work
Be_3AsF_3	3.201	4.281	78.500	0.90	−3.72	This work
Be_3SbF_3	2.158	4.565	95.166	0.85	−3.30	This work
Mg_3PBr_3	1.43	5.463	163.003	0.854	−3.35	[38]
Mg_3SbF_3	3.46	5.02	126.51	0.794	−3.18	[16]
Ba_3SbF_3	1.07	6.407	263.03	0.89	−4.59	[39]
Ca_3AsCl_3	1.742	5.756	190.7	0.849	−4.85	[40]

Table 1. Optimized structural models and associated thermodynamic stability parameters for Be_3MF_3.

computational precision and dependability of the current results. To further validate the geometric stability of the cubic structure, the Goldschmidt tolerance factor (τ_G) was computed using Eq. (1)[36].

$$\tau_G = \frac{2\,(R_A + R_X)}{\sqrt{2}\,(R_B + 2R_X)} \tag{1}$$

where R_A, R_B, and R_X specify the ionic radii of the A-site cation (Be), B-site atom (P, As, or Sb), and X-site anion (F), accordingly. The calculated tolerance factor of τ_G between 0.804 to 1 is comfortably situated within the defined stability range for cubic perovskites ($0.71 < \tau < 1.00$), affirming the maintenance of a stable cubic phase devoid of significant lattice aberrations. This geometric stability is a vital prerequisite for sustaining consistent optoelectronic properties, which are crucial for dependable device performance over prolonged operational durations. The thermodynamic stability of the Be_3MF_3 compounds was assessed by computing the formation energy (E_f) as per Eq. (2)[37].

$$E_f = E_{Be3MF3} - (3E_{Be} + E_M + 3E_F) \tag{2}$$

where E_{Be3MF3} denotes the cumulative energy of the optimum configuration, and E_{Be}, E_M and E_F correspond to the aggregate energies of the constituent Be, M, and F atoms, respectively. The negative formation energy estimates (Table 1) indicate that all Be_3MF_3 molecules are energetically favorable and thermodynamically stable, hence affirming their viability for experimental synthesis. The comprehensive evaluation of optimized lattice parameters, tolerance factor, and formation energy confirms the significant structural integrity of the Be_3MF_3 perovskites. This intrinsic stability improves their prospective incorporation into solar, optoelectronic, and advanced energy-harvesting applications, where phase resilience and minimum structural variation are essential for attaining superior device performance and operational longevity.

Electronic band structure and density of states

The electronic band structure and density of states (DOS) are essential instruments for elucidating the electronic characteristics of crystalline solids, since they disclose the distribution of electrons across different energy levels E (in eV). Examining the band structure yields essential insights into a material's conductive, semiconductive, or insulating properties, which directly influence its electrical, optical, and thermal responses. This comprehension is essential for customizing materials for sophisticated electrical applications, such as semiconductors, field-effect transistors, photodetectors, and PV cells. Figure 2a, c, e illustrates the computed band structures of Be_3MF_3 (M = P, As, Sb) compounds derived from the GGA-PBE functional. The computations were executed along high-symmetry directions (X–R–M–Γ–R) within the Brillouin zone, with the Fermi energy level (E_F) indicated by a red dashed line set at 0 eV. The valence bands are situated beneath the E_F, whilst the conduction bands are positioned above them. The lack of band overlap at E_F signifies that all Be_3MF_3 compounds possess semiconducting properties. The PBE-GGA functional, despite inherent self-interaction inaccuracies, frequently underestimates the band gap owing to its semi-local exchange–correlation characteristics. This constraint is particularly apparent in halide-based perovskites, where robust electron–electron interactions govern the electrical and optical properties[41]. Nonetheless, PBE-GGA continues to be highly proficient in capturing qualitative patterns in electrical structure and band dispersion. Advanced methodologies, including hybrid functionals (HSE06) and techniques such as GW or mBJ, enhance bandgap precision by integrating accurate exchange corrections, however they entail significantly more computational expense[42]. PBE-GGA, while producing lower absolute gap values, provides an exceptional balance between computational efficiency and physical reliability, rendering it ideal for extensive and defect-focused simulations. Its strength in consistently recreating electrical and optical trends guarantees dependable insights into structural and compositional changes in intricate perovskite systems.

The investigation of the electronic band structure indicates that the valence band maximum (VBM) and conduction band minimum (CBM) of Be_3MF_3 (M = P, As, Sb) are located at different high-symmetry points (R-G) in the Brillouin zone, hence validating their indirect band gap characteristic. The determined band gaps 3.327 eV for Be_3PF_3, 3.201 eV for Be_3AsF_3, and 2.158 eV for Be_3SbF_3, as shown in Table 1, categorize these compounds as wide-bandgap semiconductors. Indirect band gap materials demonstrate phonon-assisted electronic transitions, leading to less non-radiative recombination and extended carrier lifetimes. These attributes offer improved thermal stability, radiation resistance, and mechanical durability, which are advantageous for high-power, high-temperature, and long-lifespan electronics. Despite their reduced efficacy in light emission, these materials are exceptionally appropriate for nonlinear optical (NLO) and passive photonic applications, where accurate light

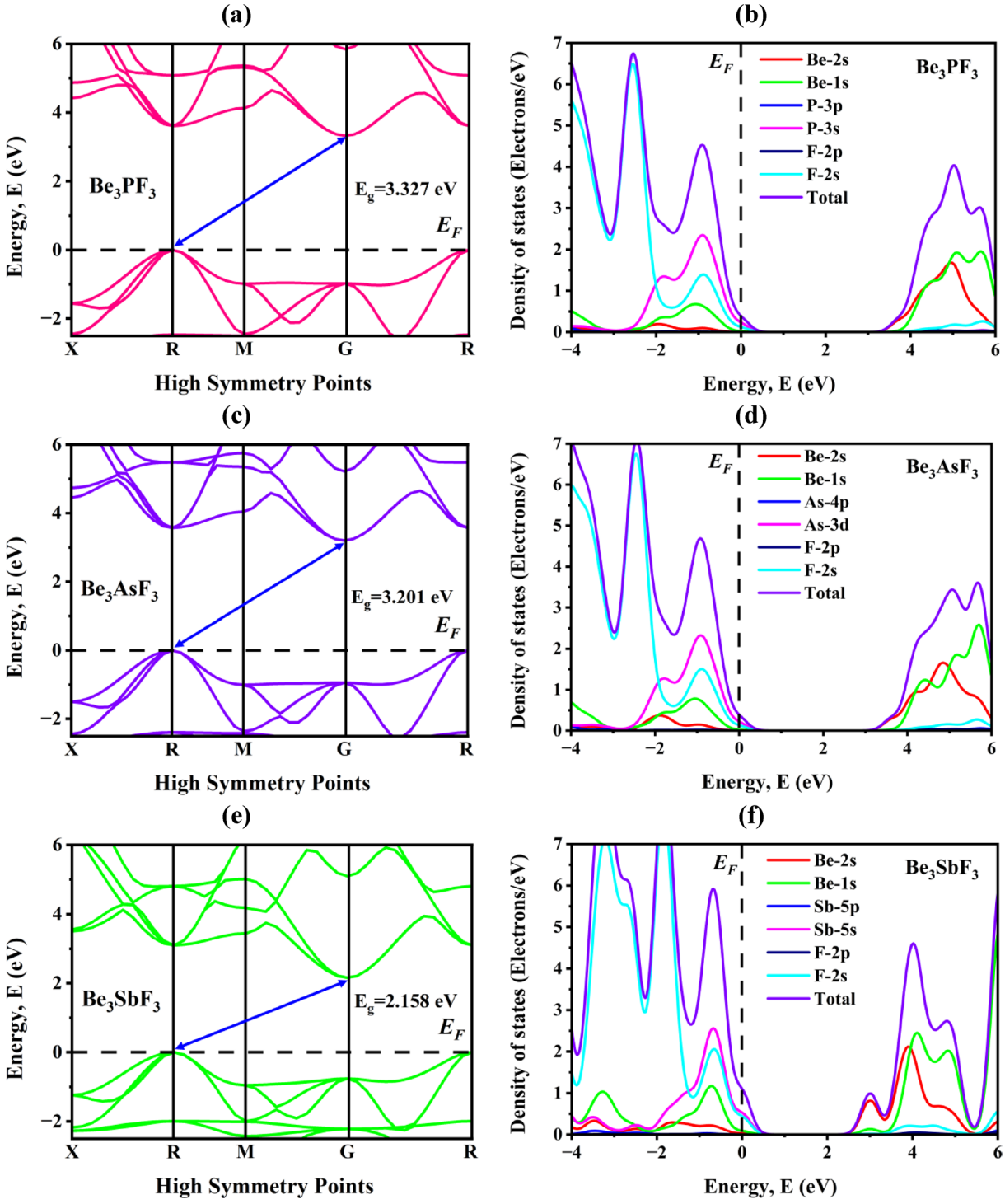

Fig. 2. The calculated electronic band structure and DOS plots for (**a**, **b**) Be_3PF_3, (**c**, **d**) Be_3AsF_3, and (**e**, **f**) Be_3SbF_3 perovskite.

modulation and elevated damage thresholds are critical[43,44]. In optoelectronic device engineering, the indirect characteristics of Be_3MF_3 compounds provide benefits for UV and deep-UV photodetectors, electro-optic modulators, waveguides, thermophotovoltaic converters, and optical limiters, where regulated light absorption and minimal recombination losses are essential. The extensive band gaps indicate robust interatomic bonding, elevated breakdown voltage, and substantial optical phonon energies, resulting in enhanced thermal conductivity and prolonged device lifespan. The intrinsic properties of Be_3MF_3 compounds render them viable candidates for energy-harvesting systems, radiation-resistant photovoltaic cells, and high-performance optoelectronic devices in sophisticated solar and photonic technologies. Among them, Be_3SbF_3 is notable for its optical transitions, substantial mechanical stability, and a moderate band gap, facilitating significant absorption throughout the

visible to near-UV spectrum. Despite its band gap being marginally greater than that of optimal single-junction absorbers, Be_3SbF_3 is still highly efficient for tandem solar cell configurations, serving as the wide-bandgap top absorber in conjunction with a low-bandgap bottom cell (such as silicon or tin-based perovskites) to expand the spectral response and improve overall efficiency[45].

The Total and Partial density of states (TDOS and PDOS) investigations offer significant insights into the electronic configuration and bonding properties of crystalline materials. TDOS provides a comprehensive overview of the total accessible electronic states across various energy levels, whereas PDOS disaggregates these contributions by specific atomic orbitals or elements, thereby clarifying the local electronic environment and the characteristics of orbital hybridization[46]. Collectively, these investigations are essential for elucidating the origins of band structure characteristics and comprehending the chemical bonding mechanisms that dictate material stability and electrical performance. Figure 2b, d, f displays the calculated TDOS and PDOS spectra for Be_3MF_3 (M = P, As, Sb) compounds, plotted against energy with E_F set at 0 eV (denoted by a black dashed line). The valence band, ranging from approximately −4 to 0 eV, is predominantly influenced by the F-2p orbitals, signifying that fluorine atoms significantly contribute to the characteristics of the upper valence band and the nature of chemical bonding.

Minor hybridization contributions from the P-3 s, As-4p, and Sb-5 s states are found near the valence band edge, indicating slight differences in electronic interactions across the series as the atomic mass of M increases. Conversely, the conduction band mostly derives from the Be-2 s and Be-2p states, supplemented by contributions from the higher-energy orbitals of group-V elements (P, As, Sb). This indicates a robust covalent interaction between Be-F and Be-M, wherein beryllium orbitals substantially affect electronic transitions and play a role in the conduction process. The extent of orbital overlap between beryllium and fluorine states suggests increased charge delocalization, potentially enhancing electron mobility and overall charge transport characteristics. The prevalence of F-2p states at the valence band maximum and Be-2 s states at the CBM confirms the indirect band gap characteristic revealed in the band structure study. The uniform electronic alignment in all three compounds emphasizes their semiconducting properties and shows the influence of fluorine and beryllium orbitals on electronic transitions. Furthermore, the progressive decline of the conduction band edge from Be_3PF_3 to Be_3SbF_3 indicates a trend of band gap shrinking, along with the augmented atomic size and diminished electronegativity of the group-V element. This electrical development is essential for optimizing optical absorption and customizing these materials for PV, photodetector, and light-emitting device applications, where precise band alignment improves energy conversion efficiency.

Optical characteristics

The optical response of a material offers essential insights into its capacity to interact with, absorb, and transmit electromagnetic radiation, which are crucial for assessing its appropriateness for photonic, optoelectronic, and PV applications. Comprehension of optical behavior is essential for materials designed for solar energy harvesting, light-emitting devices, photodetectors, and nonlinear optical systems. These features are predominantly determined by electronic structure and chemical bonding factors, which affect electron transitions between valence and conduction bands when exposed to incident light. The investigation of halide-based perovskites has proliferated in recent years owing to their exceptional light absorption, adjustable band gaps, and elevated carrier mobility. The optical properties of Be_3MF_3 (M = P, As, Sb) were examined by first-principles DFT to evaluate their applicability in advanced energy conversion and optical communication technologies. The analyzed optical functions encompass the absorption coefficient ($\alpha(\omega)$), reflectivity ($R(\omega)$), refractive index ($n(\omega)$), dielectric function ($\varepsilon(\omega)$), optical conductivity ($\sigma(\omega)$), and energy loss function ($L(\omega)$), all assessed up to 30 eV photon energy, as seen in Fig. 3a–f. These features jointly delineate the propagation of electromagnetic waves within the material and the efficiency of their interaction with photons across various frequency spectra.

The absorption coefficient ($\alpha(\omega)$) indicates the capacity of Be_3MF_3 compounds to absorb photons and generate charge carriers, as illustrated in Fig. 3a, and serves as an essential indicator of their light-harvesting effectiveness. The absorption spectra initiate at specific photon energies that align with their optical band gaps, in accordance with the semiconducting characteristics derived from band structure research. The tight correlation between electronic and optical data validates the trustworthiness and internal consistency of band structure computations[47]. Numerous pronounced absorption peaks are observable over the UV spectrum, indicating effective photon electron interactions at elevated energies. Among the compounds, Be_3PF_3 has the most pronounced absorption peak at approximately 13.62 eV with an intensity of 24.27, while Be_3AsF_3 and Be_3SbF_3 provide peaks around 23.02 and 21.7, respectively. The existence of several maxima and minima throughout the spectrum signifies intricate interband electronic transitions involving Be-F and Be-M orbital hybridizations. Despite the absorption intensity being comparatively low below 2.5 eV because to the indirect bandgap characteristics and fluorine-induced electronic localization, a pronounced rise is noted at elevated photon energies, signifying effective photon–electron coupling in the UV–visible spectrum. The notable optical activity indicates that Be_3MF_3 compounds, especially Be_3SbF_3, hold considerable promise for incorporation into UV photodetectors, radiation-resistant coatings, and tandem solar cell designs[48]. Their elevated absorption coefficients in the ultraviolet spectrum render them advantageous for high-power optoelectronic devices, UV filters, and laser protection applications, where wide bandgap materials with resilient optical responses are essential for performance and longevity.

The reflectivity, $R(\omega)$, quantifies the efficiency with which a substance reflects incoming electromagnetic radiation. This characteristic directly affects the optical contrast, thermal regulation, and energy retention of materials employed in photonic systems and solar cells. Figure 3b illustrates the reflectivity spectra of Be_3MF_3 compounds across an extensive photon energy range. At 0 eV, the reflectivity initiates at moderate levels ranging from 0.16 to 0.175, indicating the intrinsic optical density of the compounds. With increasing photon energy, reflectivity progressively ascends in the infrared and visible spectra, reaching peak values of 0.318 for

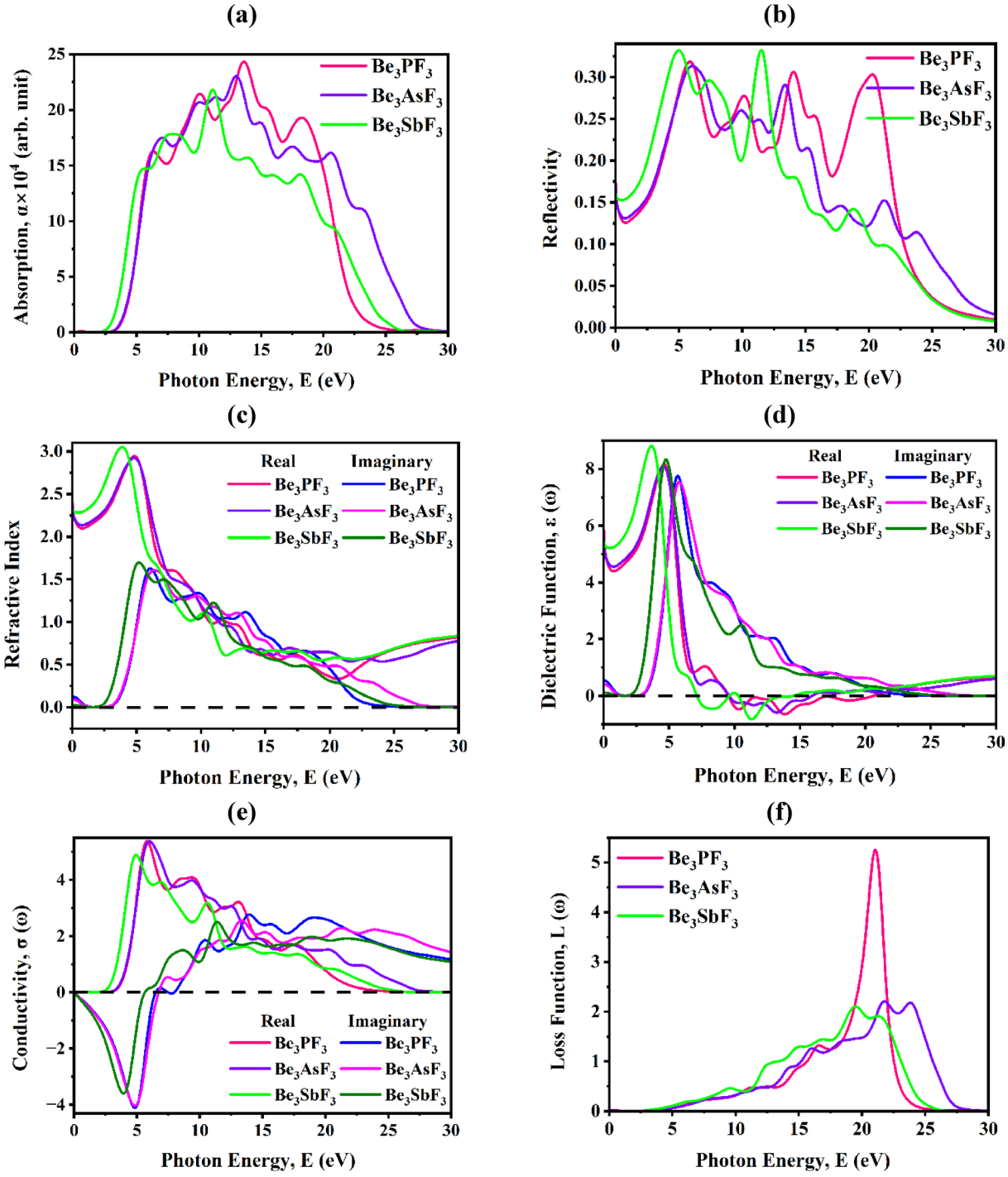

Fig. 3. The optical characteristics of Be_3MF_3 perovskite compounds encompass (**a**) absorption spectra, (**b**) reflectivity, (**c**) variations in refractive index, (**d**) the real and imaginary components of the dielectric function, (**e**) optical conductivity, and (**f**) electron energy loss function, underscoring their applicability in optoelectronic and PV domains.

Be_3PF_3, 0.313 for Be_3AsF_3, and 0.332 for Be_3SbF_3. This little difference can be ascribed to the rising atomic mass and the associated alteration in electronic polarizability of the M-site elements (P, As, Sb). At elevated photon energy (exceeding 27 eV), the reflectance of all three substances declines precipitously, nearing zero. The decreasing reflectance signifies a transparent optical window in the UV–visible spectrum, facilitating effective photon transmission through the material[49]. This optical characteristic is essential for anti-reflective coatings, transparent electrodes, and optical encapsulants utilized in PV and photonic devices, as diminished surface reflection improves energy absorption and device performance. Moreover, the prevailing tendency indicates that

the Be_3MF_3 perovskites exhibit an intrinsic equilibrium between reflection and absorption a desirable attribute for light-trapping structures in thin-film solar cells.

The refractive index, n(ω), measures the extent of light refraction as it traverses a material and offers insight into optical polarization and dielectric behavior. The real and imaginary components of n(ω) were computed, as depicted in Fig. 3c. The static refractive index values, n(0), vary from 2.3 to 2.5, indicating a modest optical density characteristic of wide band gap semiconductors. In the infrared and visible spectra, the real part of n(ω) progressively ascends, attaining peak values of 2.92 for Be_3PF_3, 2.91 for Be_3AsF_3, and 3.99 for Be_3SbF_3 within the energy range of 3.1–4.8 eV. This increase implies robust light–matter interaction and proposes possible applications in nonlinear optical modulation and light confinement systems. As photon energy increase, the refractive index progressively diminishes, signifying a reduction in transparency and a shift towards elevated optical absorption. The imaginary component of n(ω), denoting the extinction coefficient, stays minimal at elevated energies, indicating diminished photon loss due to scattering or absorption. The near resemblance in the refractive index values of Be_3PF_3 and Be_3AsF_3 suggests analogous bonding properties and electrical behaviors, whereas Be_3SbF_3, with a little elevated peak, may provide improved optical polarization due to its greater atomic size and diminished band gap. The refractive index analysis indicates that Be_3MF_3 compounds exhibit excellent optical transparency and moderate refractive properties, making them appropriate for light-guiding components, photonic waveguides, and electro-optic modulators.

The dielectric function, $\varepsilon(\omega) = \varepsilon_1(\omega) + i\varepsilon_2(\omega)$, characterizes a material's reaction to an external electromagnetic field and offers essential understanding of polarization effects and optical transition processes. The real component, $\varepsilon_1(\omega)$, signifies the dispersive (polarizable) aspect, whereas the imaginary component, $\varepsilon_2(\omega)$, pertains to absorption and energy dissipation resulting from interband transitions. The calculated dielectric spectra are displayed in Fig. 3d. At zero photon energy, the actual dielectric constant $\varepsilon_1(0)$ ranges from 5.4 to 5.9, signifying substantial electronic polarization[50]. The real component displays peak values between 8.1 and 8.9 at around 4.5 eV, indicating significant dipole excitation within this energy spectrum. The imaginary component, $\varepsilon_2(\omega)$, has pronounced peaks in the visible spectrum and progressively diminishes to zero beyond 25 eV, indicating negligible energy loss at elevated photon energies. The characteristics indicate that the Be_3MF_3 perovskites exhibit superior dielectric stability and frequency-dependent polarization regulation, essential for electro-optical modulators, optical sensors, and capacitive energy storage systems. The significant correlation between $\varepsilon_1(\omega)$ and n(ω) profiles further validates the self-consistency of the optical analysis and emphasizes the resilience of the materials' optical polarization response.

The optical conductivity (σ(ω)), measures a material's capacity to transfer charge carriers when subjected to optical excitation and is essential for evaluating photoconductive efficiency. Figure 3e illustrates the real and imaginary components of σ(ω) for the Be_3MF_3 series. The real component of σ(ω) displays distinct peaks between 4.7 and 5.3, indicating active interband transitions and effective electron excitation across the optical band gap. The analogous magnitudes among the three chemicals indicate similar electron mobility in optical fields. The imaginary component, linked to phase lag in carrier response, exhibits a gradual decrease over the infrared and visible spectra, signifying diminished reactive losses. The elevated optical conductivity in the visible spectrum indicates robust light-induced carrier excitation and effective current responsiveness when illuminated. Their attributes, along with wide band gap stability, render Be_3MF_3 materials exceptional prospects for photoconductive sensors, transparent conductors, and energy-efficient optoelectronic systems.

The energy loss function (L(ω)) indicates the energy dissipated by a high-velocity electron as it moves through a solid and offers direct insights into plasmon resonances collective oscillations of free electrons. Figure 3f depicts the loss function spectra for the Be_3MF_3 molecules. With reduced photon energies, the loss function diminishes owing to heightened photon absorption within that spectrum. Distinct plasmon resonance peaks arise at elevated energy, corresponding to plasma frequencies where collective electronic oscillations prevail[51].

The peak L(ω) for Be_3PF_3 is around 21.06 eV (≈5.25), whereas Be_3AsF_3 and Be_3SbF_3 display lower peak values of 2.2 and 2.1, respectively. The peaks signify robust electron–photon interaction and moderate energy dissipation, validating the promise of Be_3MF_3 compounds for plasmonic and photothermal applications, where regulated energy loss and resonance characteristics are beneficial. Furthermore, the comparatively low loss function at visible photon energies indicates negligible damping and superior optical quality, rendering these materials suitable for transparent coatings, UV shielding layers, and light management systems in optoelectronic devices.

Mechanical characteristics

The mechanical properties of crystalline materials are essential for comprehending their stability, deformation behavior, and applicability in industrial and optoelectronic fields. Elastic constants (C_{ij}) are essential markers of interatomic bonding strength, measuring a solid's response to external stress and strain. This study comprehensively examined the elastic characteristics of Be_3MF_3 (M = P, As, Sb) utilizing the linear finite strain–stress methodology in CASTEP. Figure 4a, b illustrates that the mechanical properties of these cubic systems are determined by three distinct elastic constants C_{11}, C_{12}, and C_{44} which correspond to resistance against uniaxial, uniform, and shear deformations, respectively. To guarantee mechanical stability, the Born-Huang stability criteria must be fulfilled[52], articulated as:

$$C_{11} + 2C_{12} > 0 \quad \text{(Spinodal criteria)}$$

$$C_{11} - C_{12} > 0 \quad \text{(Born criteria)}$$

$$C_{44} > 0 \quad \text{(Shear criteria)}$$

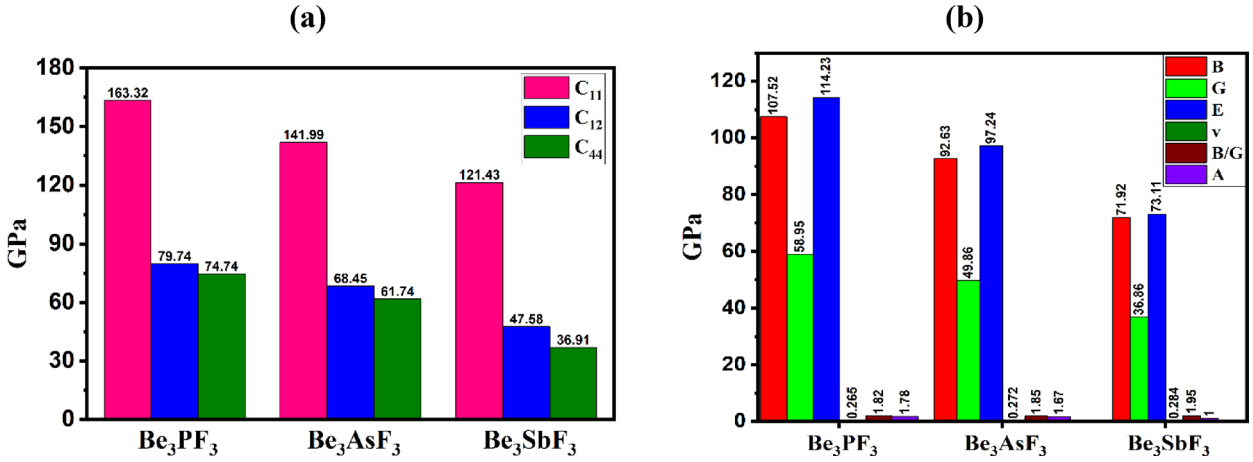

Fig. 4. Values of calculated (**a**) elastic and (**b**) mechanical constants for Be_3MF_3 (M = P, As, Sb).

Figure 4a demonstrates that all Be_3MF_3 compounds meet the mechanical stability criterion, with C_{11} significantly above C_{12} and C_{44}, signifying greater resistance to longitudinal compression compared to shear deformation. Among the series, Be_3PF_3 demonstrates the greatest C_{11} value, indicating increased bond strength and diminished compressibility, in accordance with its exceptional mechanical stiffness. The Voigt–Reuss–Hill (VRH) averaging approach was utilized to achieve a comprehensive characterization of polycrystalline mechanical behavior[53]. This approach reconciles the Voigt model (uniform strain) and the Reuss model (uniform stress), yielding a realistic estimation of the effective mechanical moduli. The bulk modulus (B), shear modulus (G), and Young's modulus (Y) were calculated using Hill's Eqs. (3–5)[54,55].

$$B = \frac{B_v + B_R}{2} \tag{3}$$

$$G = \frac{G_v + G_R}{2} \tag{4}$$

$$Y = \frac{9BG}{3B + G} \tag{5}$$

Consequently, Poisson's ratio (v) was obtained from the subsequent Eq. (6).

$$v = \frac{(3\mathrm{B} - 2\mathrm{G})}{2\,(3\mathrm{B} + \mathrm{G})} \tag{6}$$

The B measures a material's resistance to volumetric change under hydrostatic pressure, whereas the G assesses its resistance to deformation under applied shear forces. Young's modulus (Y), a critical indicator of stiffness, denotes the ratio of tensile stress to strain in the elastic range and is inversely related to thermal shock resistance. The computed findings in Fig. 4b, indicate that Be_3PF_3 demonstrates the greatest values of B, G, and Y, succeeded by Be_3AsF_3 and Be_3SbF_3. This signifies that the Be_3PF_3 compound is mechanically the most resilient, exhibiting the highest resistance to deformation and compression. The increased moduli of Be_3PF_3 indicates more robust directional bonding and reduced Be-F and Be-P bond lengths, hence augmenting lattice rigidity. In contrast, when the M-site atom enlarges (from P to when to Sb), the moduli diminish due to bond elongation and diminished charge localization, indicating fewer interatomic interactions and a marginal improvement in flexibility. Elevated values of B, G, and Y indicate that these materials possess structural integrity and mechanical stability, rendering them ideal for high-stress or high-temperature applications, including optoelectronic devices, dielectric substrates, and coating materials in solar energy systems. Pugh's ratio (B/G) and Poisson's ratio (v), which are critical parameters for differentiating ductile from brittle materials. A pivotal Pugh's ratio threshold of 1.75 distinguishes ductile (B/G > 1.75) from brittle (B/G < 1.75) behavior[56]. The computed B/G ratios for Be_3PF_3 (1.824), Be_3AsF_3 (1.858), and Be_3SbF_3 (1.951) surpass this threshold, so affirming that the complete Be_3MF_3 series demonstrates ductility. Be_3SbF_3 exhibits the highest ratio, indicating superior plastic deformability and enhanced resistance to fracture under mechanical stress. This ductility indicates that these materials can experience moderate elastic–plastic deformation prior to failure, providing robustness against stress building during thin-film development and device assembly. This inherent mechanical compliance is beneficial in the manufacturing of perovskite solar cells, where films frequently undergo stress due to thermal annealing, substrate mismatch, and multi-layer stacking. Ductile absorber layers exhibit reduced vulnerability to microcrack development and interfacial delamination, therefore preserving film continuity, grain integrity, and electrical stability throughout prolonged operation[57]. Moreover, the mechanical flexibility inherent in ductility facilitates possible incorporation into flexible or wearable optoelectronic systems, permitting Be_3MF_3 films to endure bending, rolling, and mechanical vibrations without structural deterioration. Poisson's ratio (v) offers

additional understanding of the bonding and elastic properties of these materials. Generally, $\nu > 0.26$ signifies ductility and primarily ionic bonding, while $\nu < 0.26$ denotes brittleness and covalent bonding. The calculated Poisson's ratios for Be_3PF_3, Be_3AsF_3, and Be_3SbF_3 all surpass 0.26, validating their ductile characteristics and affirming a predominantly ionic bonding structure that enhances elastic flexibility. The simultaneous presence of elevated B/G and ν values confirms that the Be_3MF_3 family integrates mechanical strength with processing suitability. This ductility improves compatibility with solution-based and vacuum deposition methods, including spin coating, sputtering, and thermal evaporation, which frequently create localized stress gradients during solvent evaporation and film cooling[58]. A supplementary metric of mechanical significance is the Zener anisotropy index (A), defined in Eq. (7).

$$A = \frac{2C_{44}}{C_{11} - C_{12}} \tag{7}$$

The calculated A values for Be_3MF_3 significantly diverge from unity, indicating considerable elastic anisotropy across crystallographic directions. Fig. S1 (Supplementary Information) illustrates that the deformed 2D and 3D elastic contour plots exhibit direction-dependent stiffness resulting from fluctuations in atomic bonding and internal stress distribution within the cubic lattice. Mechanical analysis verifies that all compounds are stable, moderately rigid, and ductile, with Be_3PF_3 demonstrating superior stiffness and Be_3SbF_3 displaying enhanced ductility. The combination of these features, along with robust ionic bonding and anisotropic elasticity, renders Be_3MF_3 materials advantageous for structural, optoelectronic, and thermomechanical applications especially in photovoltaic encapsulation, radiation-resistant optics, and high-frequency device substrates.

SCAPS 1D result

Solar cell performance evolution using Be_3SbF_3 as absorber material

Figure 5a–c depicts the fundamental structure and band alignment of a lead-free PSC, which includes ETL, HTL, and a back contact, incorporating a Be_3SbF_3 absorber layer. The device utilizes an n-i-p configuration, wherein the intrinsic Be_3SbF_3 layer creates an extensive depletion region that improves sensitivity to long-wavelength photons. This facilitates the effective creation and separation of electron–hole pairs both inside and beyond the depletion region, enhancing quantum efficiency and charge collection[59].

Moreover, Be_3SbF_3 proficiently restricts charge carriers and photons, augmenting photon absorption and establishing ohmic contacts with the doped HTL and ETL layers, so improving device performance. This device utilizes Cu_2O, P3HT, NiO, V_2O_5, MoO_3, and PTAA as HTLs, with Ni functioning as the rear metal contact and Al as the front metal contact. The employed ETLs are In_2S_3, TiO_2, Mg:ZnO, and IGZO, with Be_3SbF_3 serving as the absorber layer. The comprehensive configuration is Al/FTO/ETL/Be_3SbF_3/HTL/Ni. Tables 2 and 3 delineate the simulation input parameters for the absorber layer, ETLs, HTLs, and fluorine-doped tin oxide (FTO), whereas Table 4 presents the values for interfacial defect layers. SCAPS-1D simulations were conducted to assess the efficacy of various PSC topologies under standard operating conditions, which included the AM1.5G solar spectrum, a frequency of 1 MHz, and an ambient temperature of 300 K.

Optimization of ETL and HTL

The photovoltaic efficacy of Be_3SbF_3-based solar cells is significantly determined by the choice and interaction of appropriate electron transport layers (ETLs) and hole transport layers (HTLs), which directly affect charge extraction, recombination dynamics, and overall device efficiency. This study extensively investigated four ETLs such as TiO_2, In_2S_3, Mg:ZnO, and IGZO alongside six HTLs as Cu_2O, P3HT, NiO, V_2O_5, MoO_3, and PTAA to determine ideal configurations for Be_3SbF_3 absorbers. ETL enables electron flow from the absorber to the front electrode while preventing hole recombination, whereas the HTL effectively extracts holes toward the rear contact, providing balanced charge transport and minimizing recombination losses[65]. Figure 6a–d demonstrates that the PV characteristics: V_{OC}, J_{SC}, FF, and PCE exhibit considerable variation depending on

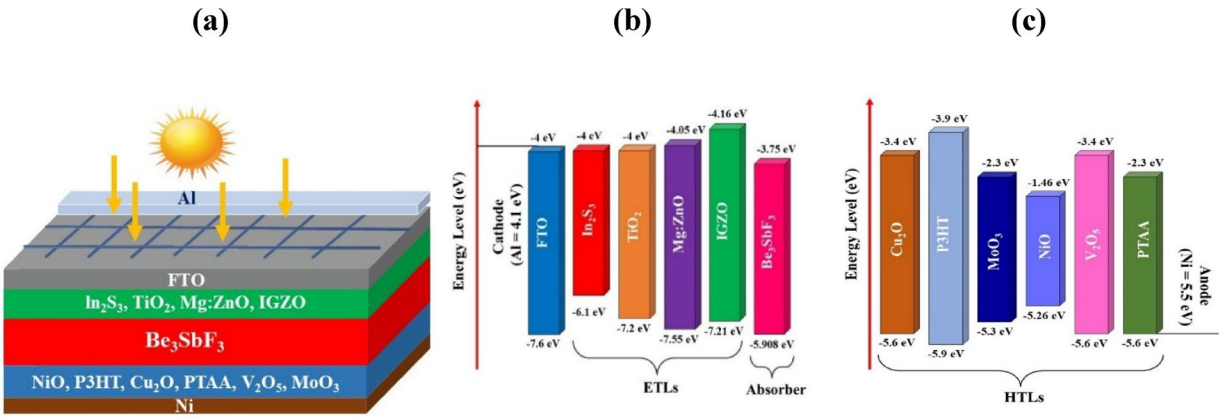

Fig. 5. Designing Be_3SbF_3-based PSCs: (**a**) device configuration and band alignment with various (**b**) ETL and (**c**) HTL materials.

Parameter (unit)	FTO	In_2S_3	TiO_2	Mg:ZnO	IGZO	Be_3SbF_3
N (μm)	0.1	0.05	0.05	0.05	0.05	1.0
Eg (eV)	3.6	2.1	3.2	3.5	3.05	2.158
χ (eV)	4	4	4	4.05	4.16	3.75
ε	9	13.5	9	8.5	10	5.45
N_V (cm^{-3})	1.8×10^{19}	4×10^{13}	1.8×10^{19}	1.8×10^{19}	5×10^{18}	7.18×10^{18}
N_C (cm^{-3})	2.2×10^{18}	1.8×10^{19}	2.2×10^{18}	2.2×10^{18}	5×10^{18}	4.17×10^{18}
μ_n ($cm^2V^{-1}s^{-1}$)	100	400	20	100	15	80
μ_h ($cm^2V^{-1}s^{-1}$)	25	210	10	25	0.1	25
N_A (cm^{-3})	0	0	0	0	0	1×10^{17}
N_D (cm^{-3})	1×10^{19}	1×10^{18}	1×10^{18}	1×10^{18}	1×10^{18}	0
N_t (cm^{-3})	1×10^{15}	1×10^{15}	1×10^{15}	1×10^{15}	1×10^{15}	1×10^{14}

Table 2. Essential input parameters for FTO, ETLs, and Be_3SbF_3 absorber layers in PSCs[51,60,61,62].

Parameter (unit)	Cu_2O	P3HT	NiO	V_2O_5	MoO_3	PTAA
N (μm)	0.1	0.1	0.1	0.1	0.1	0.1
Eg (eV)	2.2	2	3.8	2.2	3	3.3
χ (eV)	3.4	3.9	1.46	3.4	2.3	2.3
ε	7.5	3	10.7	8	18	9
N_V (cm^{-3})	1×10^{19}	1.8×10^{19}	1×10^{19}	5×10^{20}	2.2×10^{18}	1×10^{21}
N_C (cm^{-3})	2×10^{19}	2.5×10^{18}	2.8×10^{19}	9.2×10^{19}	1×10^{19}	1×10^{21}
μ_n ($cm^2V^{-1}s^{-1}$)	200	10,000	100	150	210	1
μ_h ($cm^2V^{-1}s^{-1}$)	8600	10,000	43.9	100	210	40
N_A (cm^{-3})	1×10^{20}	1×10^{20}	1×10^{20}	1×10^{20}	1×10^{20}	1×10^{20}
N_D (cm^{-3})	0	0	0	0	0	0
N_t (cm^{-3})	1×10^{15}	1×10^{15}	1×10^{15}	1×10^{15}	1×10^{15}	1×10^{15}

Table 3. Key input parameters of diverse HTLs in PSCs[63,64].

Parameter	Be_3SbF_3/ETL	HTL/Be_3SbF_3
Type of defect	Neutral	
E_r (eV)	0.6	
Energetic distribution	Single	
σ_e/σ_h (cm^2)	1×10^{-19}	
Total density (cm^{-2})	1×10^{11}	

Table 4. Investigating primary interface parameters in PSCs.

the combinations of ETL and HTL. Among the ETLs, TiO_2 attained the highest V_{OC} (about 1.80 V), whilst Mg:ZnO exhibited the lowest (about 1.61 V). In_2S_3 and IGZO yielded intermediate values, so validating their stable interfacial characteristics. For J_{SC}, most devices displayed values ranging from 9.65 to 11.04 mA/cm^2, with IGZO demonstrating a little decreased current density attributable to restricted carrier mobility and interface discrepancies. The FF varied from 86.61% (IGZO) to 91.89% (In_2S_3), with In_2S_3 identified as the most efficient electron transport layer because of its enhanced charge extraction and reduced interface recombination. Table S1 (Supplementary Information) illustrates the four most effective device architectures. The Al/FTO/In_2S_3/Be_3SbF_3/Cu_2O/Ni design achieved the best PCE of 18.28%, surpassing alternative combinations.

The Cu_2O HTL demonstrated exceptional efficacy across all ETLs, owing to its good band alignment, superior p-type conductivity, and chemical stability[66]. In contrast, NiO exhibited comparatively lower power conversion efficiencies because of suboptimal energy-level alignment. The findings underscore the necessity of sustaining optimal HTL thickness and band alignment to reduce recombination and improve carrier transmission. The integration of In_2S_3 as ETL and Cu_2O as HTL establishes an optimal interface design, delivering a synergistic equilibrium of voltage, current, and efficiency. This underscores Be_3SbF_3 promise as a durable lead-free absorber for advanced optoelectronic and PV applications.

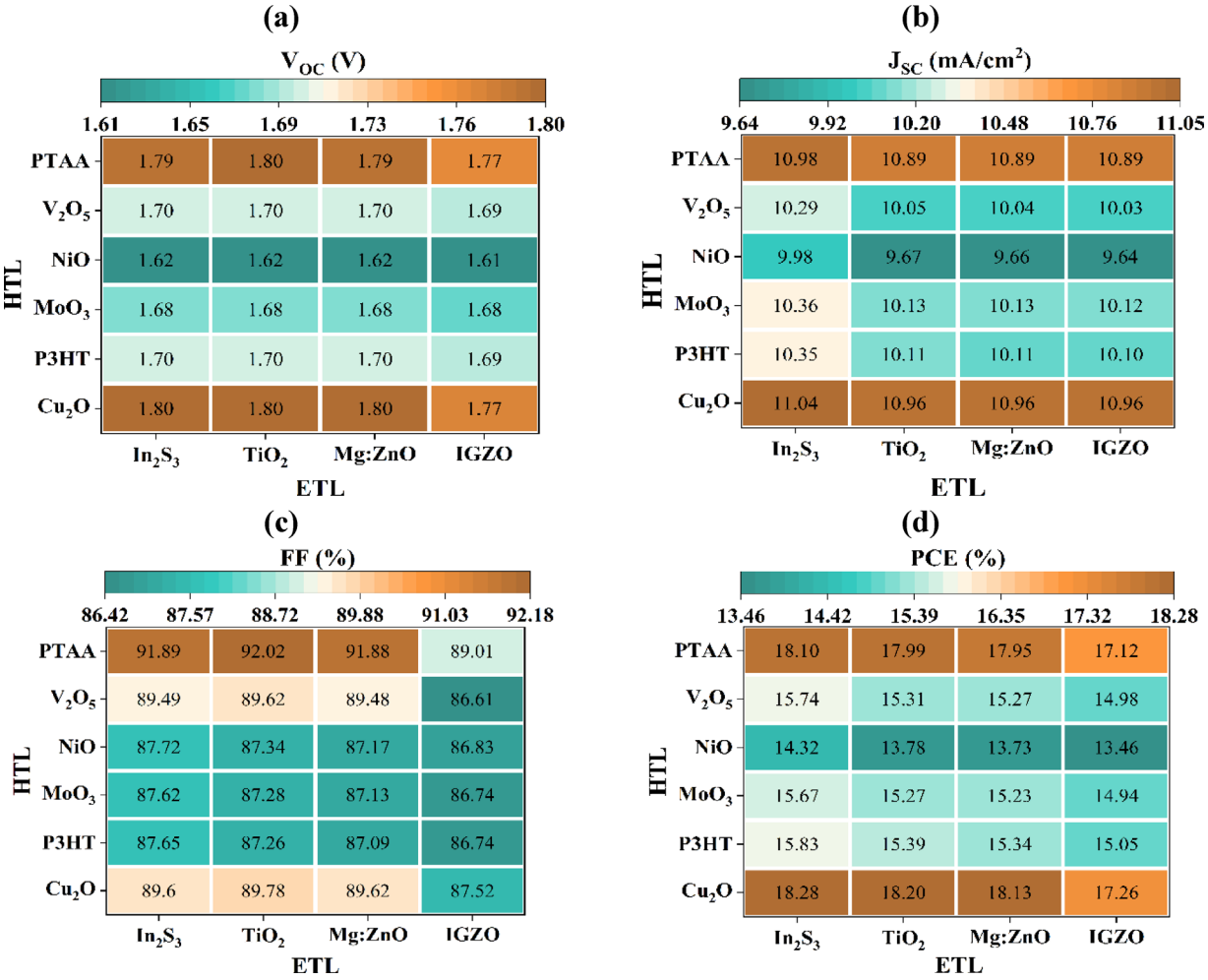

Fig. 6. Assessment of charge transport layers on critical performance metrics: (**a**) V_{OC}, (**b**) J_{SC}, (**c**) FF, and (**d**) PCE in Be_3SbF_3 SCs.

Role of back contact work function in determining solar cell characteristics

Back contact is crucial in influencing solar cell efficiency and overall performance. It must minimize resistive losses to ensure efficient current extraction, as inadequate contact elevates series resistance and diminishes power production[67]. Moreover, robust adhesion and chemical stability with the semiconductor are essential for the longevity of the device. Poor design may result in shade and restrict the effective area for energy conversion. An improved back contact enhances charge carrier collection, reduces recombination losses, and consequently improves the performance and dependability of the solar cell. The optimal metal for back contact is primarily determined by its work function (WF), which varies from 4.81 eV to 5.9 eV, as detailed in Table S2. Fig. S2 depicts the PV parameters acquired with diverse back contacts for distinct ETLs. The findings demonstrate that a reduction in WF of the Fe contact corresponds to a decline in the PCE of the SC. An elevation in WFs of metals like Au, Ni, Pd, Pt, and Se demonstrates a consistent positive link with improved PCE. This enhancement is primarily ascribed to the diminution of the Schottky barrier height via improved alignment of the metal work function with the Fermi level of the HTL[68]. Ni is the most appropriate back contact material among these metals, owing to its ideal work function, cost efficiency, plentiful availability, and consistent performance, rendering it a viable option for efficient and scalable device manufacturing.

Energy band diagram (EBD) of Be_3SbF_3

The energy band diagram (EBD) illustrates the conduction and valence band offsets (E_C and E_V) between the Be_3SbF_3 absorber and the HTL, influenced by various ETLs in conjunction with Cu_2O. Optimal energy level alignment at the ETL/Be_3SbF_3 and Be_3SbF_3/HTL interfaces is essential for maximizing device efficiency. Misalignment may result in charge accumulation and interfacial recombination, thereby diminishing performance. For efficient operation, ETL must exhibit a higher electron affinity than Be_3SbF_3 to enable effective electron extraction, whereas HTL should demonstrate a lower ionization energy to promote hole transport[69]. Therefore, optimizing the interfacial electronic properties of both layers is crucial for improving overall PV efficiency. Figure 7a–d illustrates the EBDs of Be_3SbF_3-based solar cell structures that utilize Cu_2O as HTL alongside four different ETLs. The configuration employing In_2S_3 as ETL shows a clear intersection of the

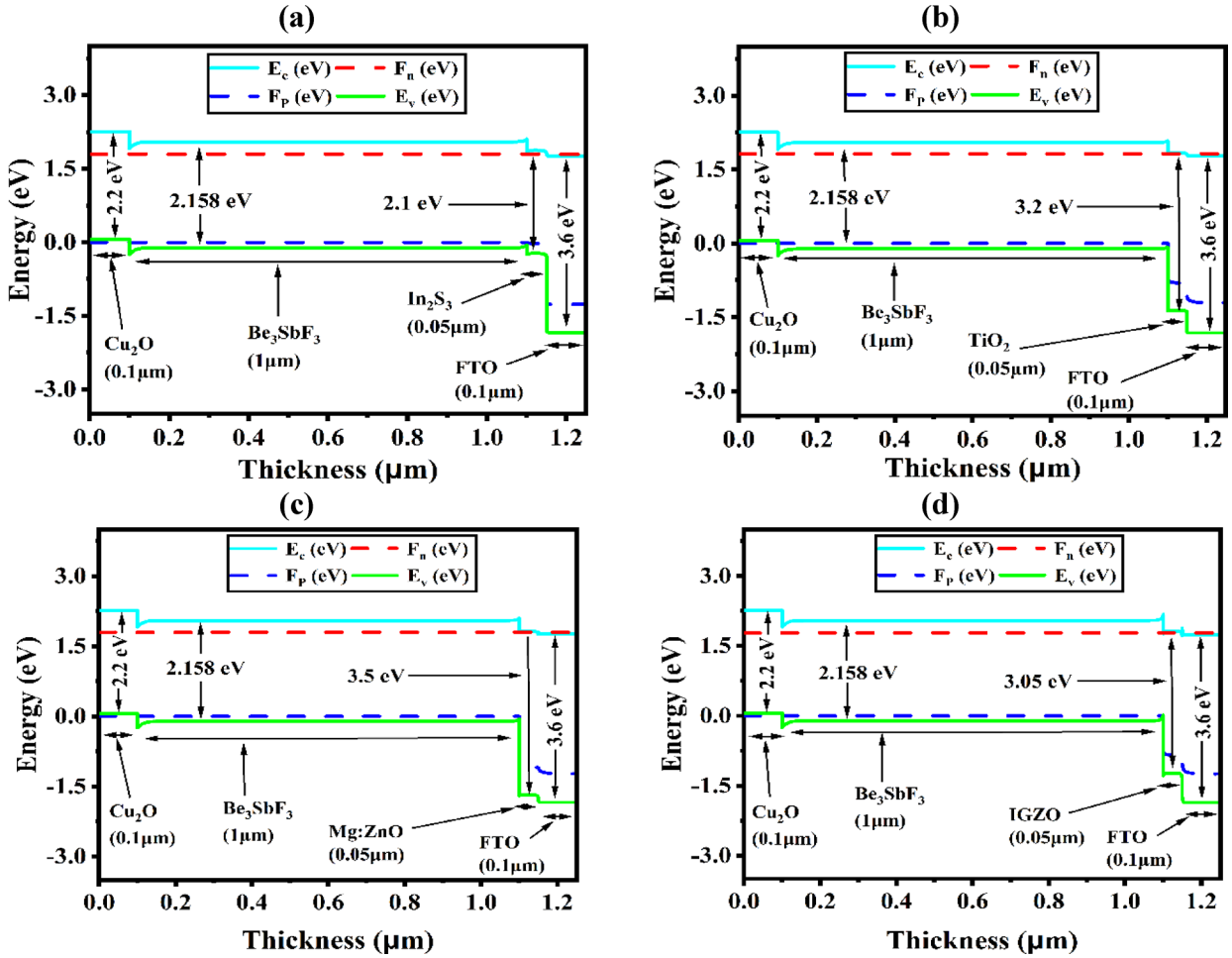

Fig. 7. Investigating variations in band structure of SCs with diverse ETLs: (**a**) In_2S_3, (**b**) TiO_2, (**c**) Mg:ZnO, and (**d**) IGZO.

Fermi level with the E_C. The ETLs utilized in these devices, ordered by ascending bandgap energy, include In_2S_3 (2.1 eV), TiO_2 (3.2 eV), IGZO (3.05 eV), and Mg:ZnO (3.5 eV). The quasi-Fermi level for holes (F_p) is consistently positioned above EV, whereas the quasi-Fermi level for electrons (F_n) is closely aligned with E_C, demonstrating effective charge carrier separation in all configurations.

Role of acceptor density and absorber thickness variations in SC performance

The dynamics of charge carriers, recombination rates, and efficiency in PSCs are significantly influenced by the acceptor density (N_A) and the thickness of the absorber layer. An optimal N_A enhances the built-in electric field, facilitating charge separation and minimizing recombination, while values that are too low or too high may impede carrier collection or elevate trap-assisted losses[70]. Thicker absorber layers enhance light absorption but may elevate recombination and resistance, while thinner layers reduce recombination but limit photocurrent[71]. Attaining an appropriate equilibrium of N_A and thickness is essential for maximizing PCE, achieved by interface engineering, doping regulation, and defect passivation to enhance stability and performance. Figure 8a–d illustrates the synergistic impact of N_A and absorber thickness on the PCE of the SCs. This study altered N_A from 10^{13} to 10^{19} cm^{-3} and adjusted absorber thickness between 0.3 and 3.0 μm. The findings reveal a notable fluctuation in PCE corresponding to alterations in these two parameters across four distinct SCs including FTO/ETL/Be_3SbF_3/Cu_2O/Ni configurations, utilizing ETLs of In_2S_3, TiO_2, Mg:ZnO, and IGZO. The PCE is generally reduced when the N_A is beneath 10^{17} cm^{-3}. When the N_A attains 10^{17} cm^{-3}, the PCE hits its zenith, signifying that elevated doping concentrations result in augmented recombination losses. As N_A surpasses 10^{17} cm^{-3}, the PCE progressively diminishes. Likewise, for absorber thicknesses between 0.5 and 1.2 μm, the PCE stays elevated but diminishes for thicker absorbers (1.5 to 3.0 μm) due to heightened bulk recombination and series resistance. Among the studied ETLs, the In_2S_3-based design (Fig. 8a) exhibited the highest PCE of around 18.28%, indicating effective charge transport and decreased recombination. The TiO_2-based (Fig. 8b) and Mg:ZnO-based (Fig. 8c)) SCs had PCE values of 18.20% and 18.15%, respectively, indicating a close similarity. The IGZO-based SC (Fig. 8d) exhibited a marginally reduced efficiency of around 17.26%, presumably attributable to fluctuations in carrier extraction characteristics. The results emphasize the importance of absorber thickness, N_A, and the selection of ETL in optimizing PCE. Achieving a balance between low N_A and moderate thickness is

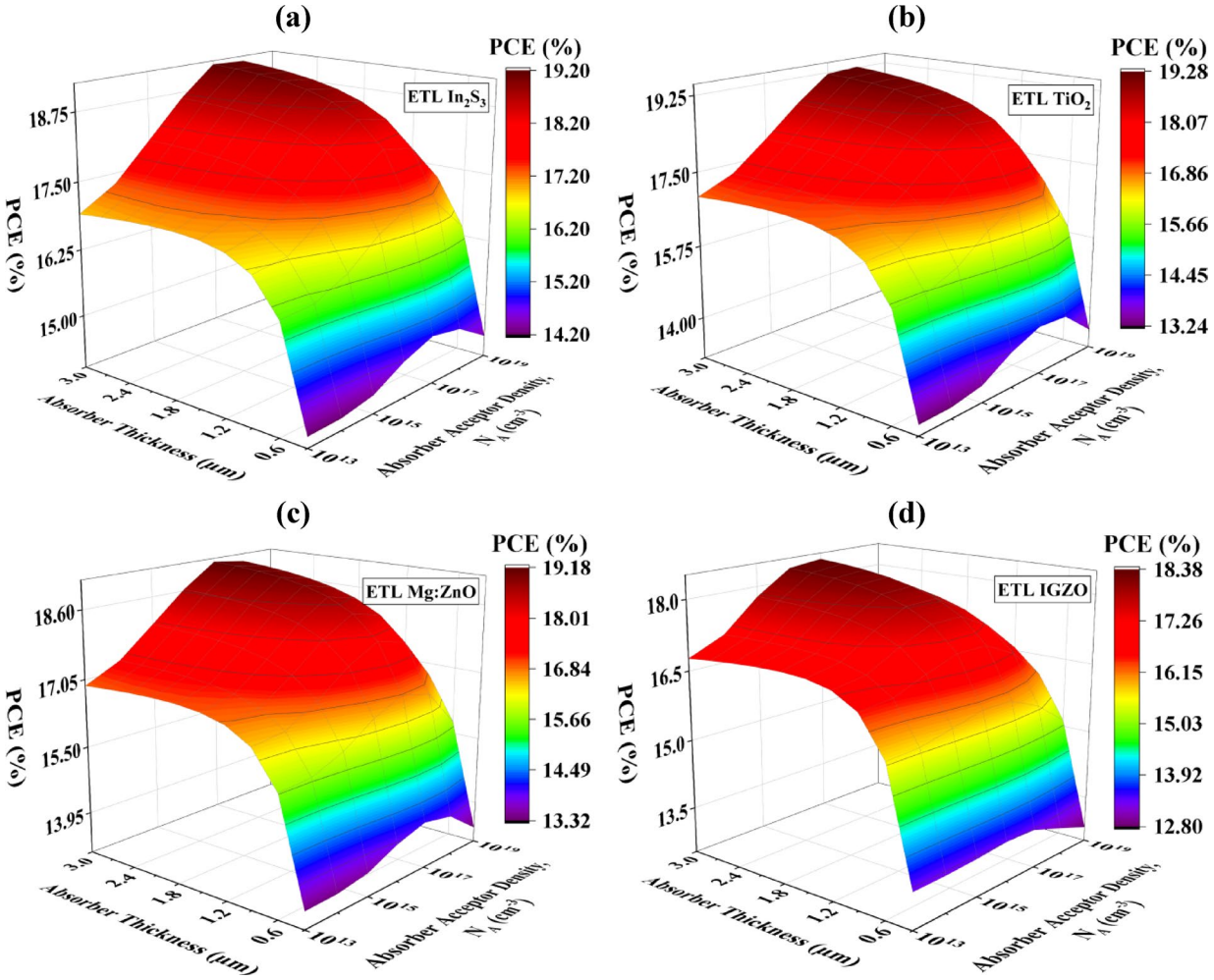

Fig. 8. Exploration of PCE fluctuation in relation to absorber layer thickness and N_A for SCs utilizing various ETLs: (**a**) In_2S_3, (**b**) TiO_2, (**c**) Mg:ZnO, and (**d**) IGZO.

essential for minimizing recombination and enhancing charge collection efficiency. Among the assessed ETLs, In_2S_3 exhibited exceptional performance in attaining elevated PCE, establishing it as a viable alternative for the advancement of high-efficiency and robust PSC designs.

Bulk and interfacial defect investigation

Organic and inorganic devices are significantly impacted by bulk defects, which are a significant factor contributing to their lower performance. The densities of defect levels are significantly influenced by experimental processing parameters; nonetheless, evaluating device performance at different defect energy levels and concentrations offers a useful comparison framework for optimizing these conditions[72]. Figure 9a–f depicts the fluctuation in solar output parameters (PCE) relative to defect energy and concentration. In the bulk defect study of the absorber layer, the defect energy level for Be_3SbF_3 was modified from − 0.2 to 2.4 eV, and the defect concentration (N_t) was altered between 10^{12} and 10^{18} cm^{-3}.

The defect energy range (− 0.2 to 2.4 eV) encompasses both shallow and deep-level trap states, facilitating a thorough examination of defect-assisted recombination in Be_3SbF_3. Shallow traps near the band boundaries (about − 0.2 eV) induce minor carrier trapping, whereas deep traps (approximately 2.4 eV) function as non-radiative recombination centers that diminish carrier lifespan and voltage. This range aligns with prior research by Reza et al.[73] and others on lead-free perovskites ($CaRbCl_3$, Ca_3NCl_3), which indicated that deep-level defects (> 2 eV) substantially impair charge collection and solar efficiency[74]. Figure 9a illustrates the associated defect energy levels and N_t for Be_3SbF_3. The data indicates that elevated N_t can significantly impact device performance. Decreasing N_t to 10^{14} cm^{-3} yields an enhancement of device performance by as much as 40%. Nonetheless, attaining such a minimal N_t is still impractical within the limitations of conventional thin-film deposition methods. Consequently, N_t of 10^{15} cm^{-3} is deemed a more plausible concentration for this investigation.

Interface defects significantly affect device performance. Figure 9b–f illustrates the examination of defect concentrations at the ETL/absorber and Cu_2O/absorber interfaces. The device's performance is analyzed at different defect concentrations and energy levels. Defect concentrations were changed from 10^{10} to 10^{16} cm^{-3}, whereas defect energy levels spanned from − 0.4 to 2.4 eV. The findings demonstrate that defects at the HTL/

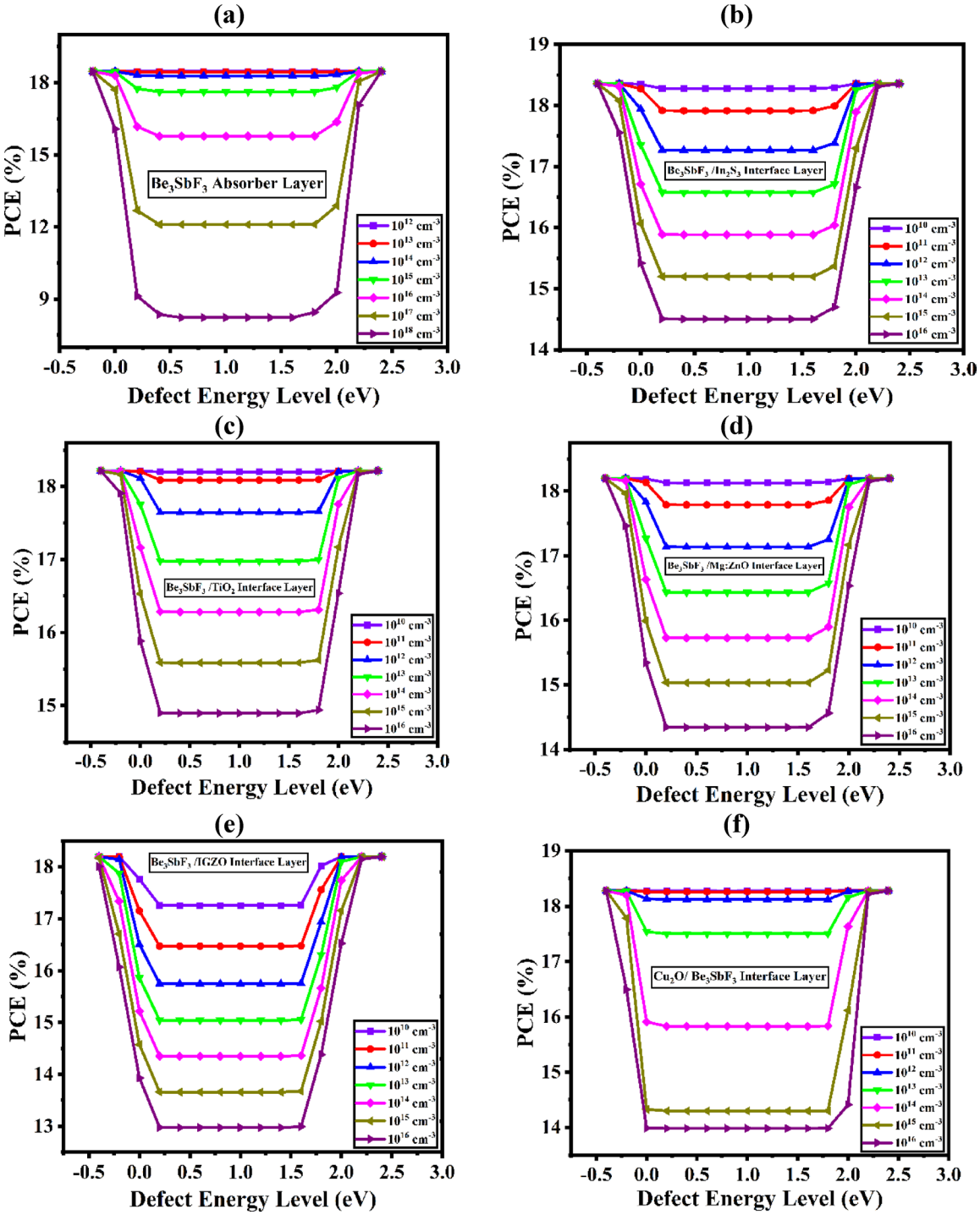

Fig. 9. Performance Analysis of SCs in various layer configurations with varying defect position and density: (**a**) Be_3SbF_3, (**b**) Be_3SbF_3/In_2S_3, (**c**) Be_3SbF_3/TiO_2, (**d**) Be_3SbF_3/Mg:ZnO, (**e**) Be_3SbF_3/IGZO, and (**f**) Cu_2O/Be_3SbF_3.

absorber interface adversely impact device performance more significantly than those at the ETL/absorber interface. The examination of bulk and interfacial defects elucidates the impact of different defects on overall device performance. In the device bulk layer, defects with energy levels ranging from 0.3 to 2 eV are categorized as deep defects, which adversely impact performance and should be eliminated. Conversely, defects at the absorber/HTL interface, exhibiting energy levels between 0 and 2 eV, are also classified as deep defects. The severity of defects in PV performance is contingent upon the location, concentration, and energy level of each defect, highlighting the necessity of meticulous defect control to enhance device efficiency.

Impact of temperature on PV efficiency

Temperature is crucial in influencing the operational stability and performance of PSCs. Although PSCs provide high efficiency and manufacturing simplicity, their large-scale production encounters obstacles, especially from environmental conditions including UV radiation, temperature variations, wetness, and humidity. Temperature is particularly crucial, as solar cells often operate in direct sunshine, where temperatures can exceed ambient values by as much as 45 °C[75]. An elevation in temperature results in a reduction of the semiconductor bandgap owing to the expansion of interatomic distances inside the material. The working temperature fluctuates for PSCs extends from 275 to 450 K, allowing for the evaluation of temperature fluctuations on cell performance. Figure 10 illustrates that temperature increase consistently diminishes critical metrics, such as V_{OC}, FF, and PCE, across all cell configurations. Notably, the J_{SC} exhibits remarkable stability despite rising temperatures. The noted reduction in V_{OC} is chiefly due to its inverse correlation with the saturation current density (J_0), which demonstrates a significant increase with rising temperature. The temperature-induced increase in J_0 arises from heightened carrier recombination rates in the absorber layer and at the interface regions[76]. The PCE and FF often decrease with elevated temperature, mainly due to the increase in series resistance and augmented non-radiative recombination losses, both of which impede efficient charge transfer and extraction[77]. Conversely, the IGZO-based device exhibits a nearly constant FF, indicating its enhanced thermal and electrical stability compared to alternative ETLs. This stability arises from IGZO enhanced electron mobility, minimal intrinsic defect density, and extensive bandgap (~3.05 eV), which together inhibit thermally induced carrier leakage and maintain the built-in electric field at high temperatures[78].

Moreover, IGZO offers a properly oriented conduction band and a chemically stable interface with the perovskite absorber, mitigating temperature-induced interfacial deterioration. Nonetheless, as temperature escalates, the concomitant increase in series resistance diminishes overall device efficiency and fill factor, resulting in a significant decline in power conversion efficiency. These findings underscore the significance of heat management in sustaining consistent performance of PSCs under practical operating situations.

Nyquist plot analysis

Impedance analysis is an effective method for examining the properties of perovskite materials, especially those containing different halides. This method is recognized as one of the most efficacious techniques for investigating the behavior of perovskite materials with various halide compositions[79]. To enhance comprehension of the effects of different ETLs on critical PV parameters, including V_{OC}, J_{SC}, FF, and PCE obtained from the I-V characteristics, complex impedance (Z^*) was utilized to investigate the influence of ion migration and charge carrier dynamics within the perovskite solar cell. Figure 11 displays the Nyquist plot of complex impedance, depicting the correlation between the imaginary component (Z_{im}) and the real component (Z_{re}) of impedance for various ETL materials. The X-axis denotes recombination resistance, but the Y-axis illustrates geometrical capacitance, indicating charge carrier concentration at the interface layers. Each curve in the graph approximates a semi-circle within the frequency spectrum of 100 Hz to 1 MHz. The real (Z_{re}) and imaginary (Z_{im}) components of the impedance are graphed against one another, revealing that the impedance spectra for each ETL exhibits a different, approximately semi-circular form. Furthermore, the diameter of the semi-circle differs among various

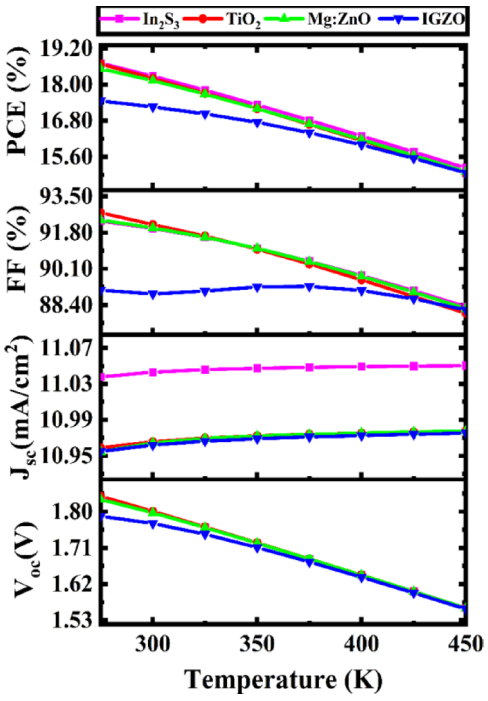

Fig. 10. Temperature-driven performance variations in PV cells with distinct ETLs.

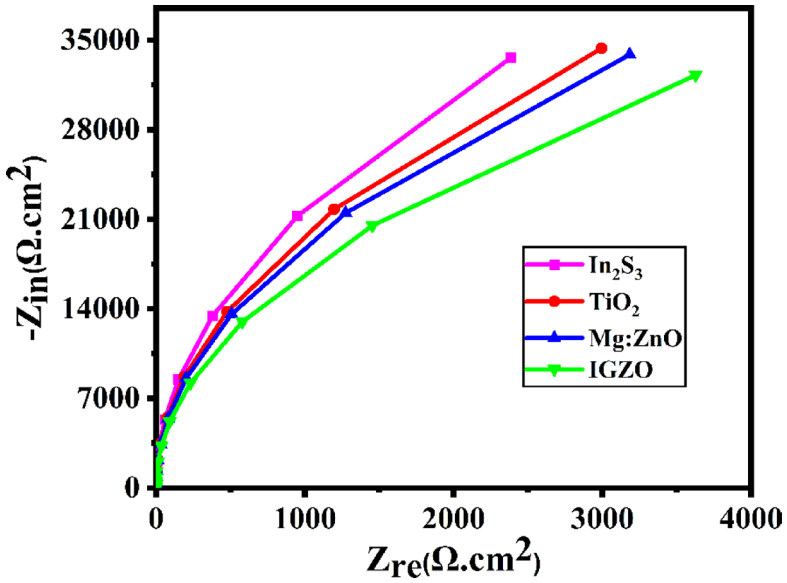

Fig. 11. Impedance analysis of Be_3SbF_3 absorber-based solar cells employing various ETL materials (In_2S_3, TiO_2, Mg:ZnO, and IGZO) via Nyquist plot.

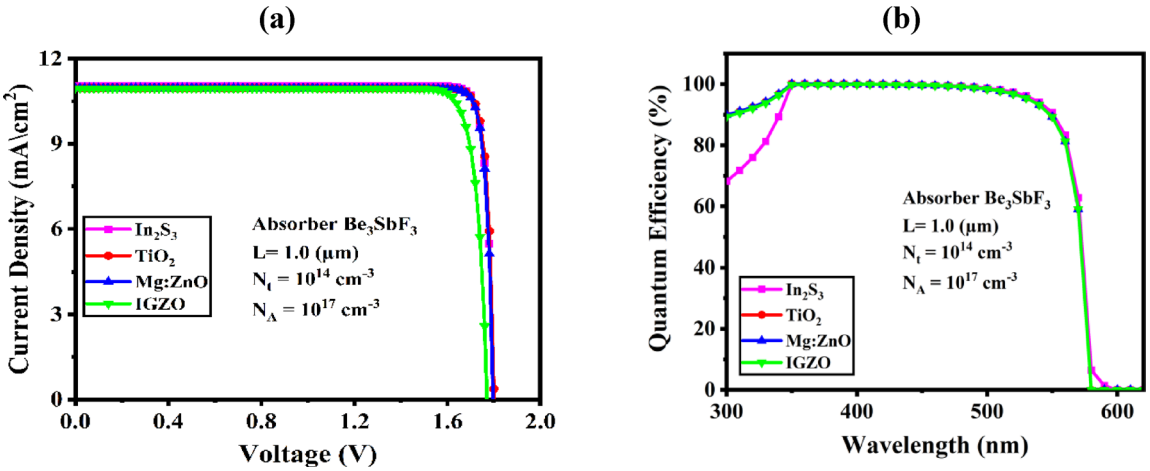

Fig. 12. Analysis of (**a**) J-V and (**b**) QE characteristics curve of PSCs.

ETL-based structures, signifying variations in electrical properties and potential performance consequences. The diameter of the semi-circle expands with increasing frequencies. The broader semi-circle linked to the TiO_2 ETL-based PSC indicates an elevated impedance of roughly 34,366.681 Ω cm^2. This indicates increased resistance inside the system, probably attributable to diminished charge transport kinetics or heightened charge transfer resistance at the perovskite-TiO_2 interface. The smaller semi-circle seen in the IGZO ETL-based structure suggests reduced resistance, approximately 32,272.6149 Ω cm^2, implying enhanced charge transfer, superior interface qualities, or more charge carrier mobility relative to other ETL materials.

At elevated frequencies, the observed resistance indicates the recombination resistance of the material, but the capacitance at these frequencies denotes the geometric capacitance, which relates to charge accumulation at the interfaces. The low-frequency response is intricate, probably reflecting ionic mobility and hysteresis phenomena[80]. As ions collect and the reduction barriers diminish, the impedance response becomes inductive. The Nyquist plot of the solar cell provides a thorough qualitative insight into the device's capacitance, resistive losses, and the rate of recombination faults present inside the device. This investigation offers critical insights into the electrical characteristics and efficiency of PSCs, enhancing comprehension of the elements affecting their performance.

J-V and QE characteristics

Figure 12a presents the J-V characteristics of four configurations of Be_3SbF_3-based solar cells under applied voltages from 0 to 2.0 V. Initially, all devices demonstrate comparable photocurrent values of approximately

11.03 mA/cm^2, except for the IGZO-based configuration, which exhibits a significantly lower current density. With an increase in voltage beyond 1.6 V, all structures exhibit a reduction in photocurrent, mainly due to increased charge carrier recombination linked to defect states in the perovskite absorber. The observations indicate that improved crystallinity and reduced defect density in the absorber layer enhance PV performance by facilitating efficient charge separation and transport.

Figure 12b illustrates the quantum efficiency (QE) spectra of Be_3SbF_3-based solar cells employing different ETLs across the 300–620 nm wavelength range. The In_2S_3-based device initiates with a reduced quantum efficiency of approximately 68%, whereas other ETL designs commence at approximately 89.9%, signifying enhanced carrier collection near the absorption edge. The QE increases significantly between 350–530 nm, exceeding 95%, indicating robust optical absorption and effective charge production. This plateau indicates superior interfacial charge transport and negligible recombination losses at optimal photon energy. Nonetheless, QE diminishes beyond 590 nm owing to non-radiative recombination and free-carrier absorption in the doped front and ETLs phenomena characteristic of wide-bandgap perovskite and oxide-based devices[81]. The spectral variations among ETLs result from disparities in band alignment, carrier mobility, and interface defect density, which significantly affect charge extraction performance. The significant quantum efficiency in the visible spectrum validates the robust optoelectronic coupling and effective photo response of Be_3SbF_3, underscoring its potential as a lead-free perovskite absorber for high-performance photovoltaic applications.

An evaluation and comparison of SCAPS-1D findings with prior studies

This study obtained remarkable performance metrics for the Al/FTO/ETL/Be_3SbF_3/HTL/Ni SC configuration. The study concentrated on integrating diverse ETLs, including In_2S_3, TiO_2, Mg:ZnO, and IGZO, into the device architecture, with Cu_2O functioning as the HTL. The systematic optimization of essential parameters, including layer thickness, doping, defect densities, temperature, J-V, and QE properties, was conducted. After optimizing these variables, the proposed structure exhibited exceptional PV performance, attaining an efficiency of 18.28%, a V_{OC} of 1.7991 V, a J_{SC} of 11.0423 mA/cm^2, and an FF of 92%. Although achieving this high PV performance may provide difficulties for experimental researchers, this study offers a framework and guidance for future inquiries. The efficacy of SCs is predominantly determined by structural design, material quality, and production methodologies. Table 5 compares the best configurations documented in prior studies with the PV characteristics of the four device types introduced in this research.

Machine learning analysis

Machine learning (ML) has significantly transformed PV research, facilitating swift, data-driven progress in PSCs. Conventional experimental and computational approaches tend to be time-consuming and resource-demanding, while machine learning techniques effectively analyze extensive datasets to identify patterns, forecast performance parameters, and inform material and structural optimization. This capability is essential for PSCs, as efficiency relies on the complex interactions among composition, processing conditions, and device architecture. Machine learning models are essential for predicting PV parameters. Researchers optimize electron and hole transport layers, absorber materials, and interface properties by integrating machine learning

Model	Types of work	PCE (%)	V_{OC} (V)	J_{SC} (mA/cm^2)	FF (%)	Refs.
$MoSe_2$/Si	E	0.33	0.19	5.71	30.47	[82]
FTO/TiO_2/Sb_2Se_3/Au	E	2.26	0.52	10.3	42.3	[83]
SLG/Mo/Sb_2Se_3/CdS/ZnO/ITO/Ag	E	4.22	0.453	19.8	50.6	[84]
TiO_2/$CsPbBr_3$/Spiro-OMETAD	E	6.08	1.307	6.820	68	[85]
$CsPbI_3$/$FAPbI_3$	E	15.60	1.22	17.26	74	[86]
$CsPbI_3$/ $Cs_{0.25}FA_{0.75}PbI_3$	E	17.39	1.20	18.91	76.00	[87]
FTO/SnS_2/Ca_3PBr_3/Au	T	13.66	1.25	12.43	87.18	[21]
FTO/TiO_2/Ca_3AsCl_3/Ni	T	17.11	1.34	14.80	86.23	[88]
C_{60}/$CsGeI_3$/CuSCN	T	17.61	1.0169	19.653	88.13	[89]
FTO/TiO_2/$RbGeI_3$/CuI/Au	T	18.97	0.777	33.969	71.93	[90]
FTO/TiO_2/Cs_2SnBr_6/N-doped TiO_2/Au	T	38.70	1.29	33.34	90.21	[91]
FTO/TiO_2/$RbGeI_3$/P3HT/Au	T	18.44	0.813	30.84	74.19	[92]
Al/FTO/SnS_2/Sr_3NCl_3 /Au	T	18.11	1.24	16.79	86.44	[93]
Al/FTO/SnS_2/Sr_3SbCl_3/Ni	T	16.63	1.364	13.738	88.74	[94]
Al/FTO/SnS_2/Ca_3SbI_3/Au	T	19.47	1.1631	19.07	87.79	[95]
Al/FTO/SnS_2/Sr_3SbI_3/MoO_3/Ni	T	17.12	0.72	29.57	80.61	[96]
Al/FTO/In_2S_3/Be_3SbF_3/Cu_2O/Ni	T	18.28	1.7991	11.042	92	T.W
Al/FTO/TiO_2/ Be_3SbF_3/Cu_2O/Ni	T	18.20	1.8009	10.963	92.18	T.W
Al/FTO/Mg:ZnO/Be_3SbF_3/Cu_2O/Ni	T	18.13	1.7972	10.961	92.02	T.W
Al/FTO/IGZO/ Be_3SbF_3/Cu_2O/Ni	T	17.26	1.7707	1.77	88.92	T.W

Table 5. A comparative assessment of PV performance in Be_3SbF_3-based PSCs: insights from previous research (T = Theoretical, E = Experimental, and T.W. = This Work).

with simulation tools such as SCAPS-1D to reduce losses. Research conducted by Shrivastav et al.[97], Khan et al.[98], and Li et al.[99] illustrates the efficacy of machine learning in enhancing lead-free and heterojunction PSCs, resulting in elevated predictive accuracy and increased efficiency. The Random Forest (RF) algorithm is notable among machine learning methods for its robustness, interpretability, and capacity to manage nonlinear, multivariate data. RF models demonstrate superior capability in identifying key parameters that influence PSC performance, frequently surpassing linear regression, support vector machines (SVM), and k-nearest neighbors (KNN) models. Advanced techniques, including Gradient Boosting, XGBoost, Artificial Neural Networks, and Deep Learning, enhance the capabilities of machine learning in high-throughput screening and autonomous material discovery[100]. The incorporation of machine learning, particularly random forests, into polymer science and engineering research signifies a transition towards intelligent and automated material optimization. The integration of statistical learning, physical modeling, and experimental insights facilitates the accelerated design of efficient, stable, and sustainable perovskite materials, thereby advancing the development of next-generation lead-free solar technologies.

Comprehending the RF algorithm

This study utilized RF technique as the primary machine learning model due to its remarkable proficiency in managing nonlinear interactions, high-dimensional feature spaces, and intricate correlations among PV parameters. The RF approach functions by creating a collection of many decision trees, each trained on randomly chosen subsets of data and input attributes. The ultimate forecast is derived by averaging the outputs of various trees, which successfully reduces overfitting while preserving excellent predictive accuracy. This ensemble-based methodology offers a dependable equilibrium among robustness, precision, and interpretability, rendering it particularly appropriates for evaluating the interaction of material, structural, and operational elements that collectively affect solar cell efficiency[101,102]. The SCAPS-1D simulator was employed to methodically alter essential device parameters, such as absorber layer thickness, electron affinity, defect and doping density, interface defect, bandgap, and operational temperature, to create a comprehensive dataset. This simulation campaign produced 13,113 data points, with 80% (10,490 samples) designated for model training and 20% (2623 samples) for testing and validation. The predictive performance of the trained RF model was assessed using the coefficient of determination (R^2) and mean absolute error (MAE) metrics, both indicating the model's robust capacity to reliably predict PV performance based on input data. The RF algorithm's primary advantage is its capacity to quantify feature importance, therefore pinpointing the most significant elements affecting PSC efficiency. This feature analysis allows researchers to prioritize elements for further optimization. The hyperparameter tweaking process was conducted with precision to guarantee optimal model performance. The model utilized 100 decision trees, attaining an equilibrium between computational efficiency and precision. The maximum tree depth was limited to avoid overfitting, and a minimum of two samples per leaf node was mandated to guarantee significant splits. Furthermore, bootstrap sampling and feature subsampling methods were employed to incorporate randomness, improve model stability, and avert the dominance of any feature in the learning process.

Figure 13 depicts the significance of essential physical parameters affecting the performance. Each bar illustrates the contribution of a particular variable to the overall PCE and electrical attributes. Bandgap energy is the most crucial element, highlighting its pivotal function in regulating light absorption, carrier production, and voltage output. An adjusted bandgap guarantees a balance between extensive spectrum absorption and reduced thermalization losses, hence directly improving J_{SC} and V_{OC}[103]. The interface defect density significantly affects the system, suggesting that non-radiative recombination at the absorber/transport layer junctions is a major loss mechanism. Mitigating interface defects via surface passivation or lattice matching can significantly improve charge extraction efficiency. Parameters like absorber thickness and acceptor density exhibit mild effects, as they affect optical absorption depth and the intensity of the internal electric field. In contrast, electron

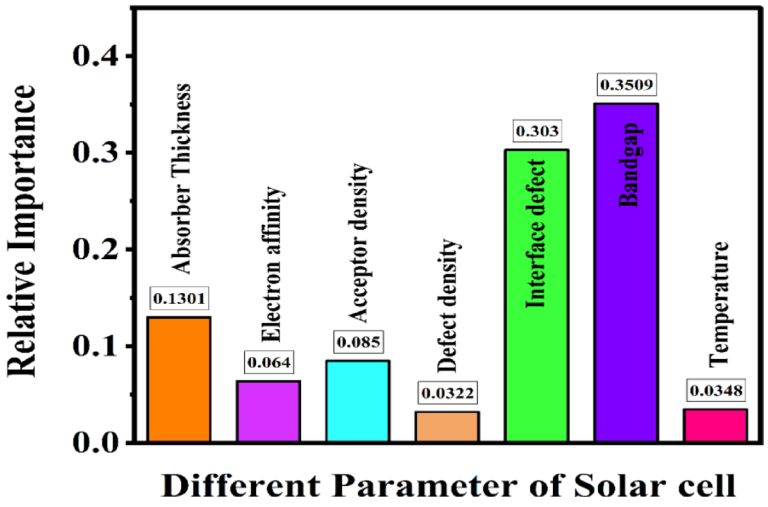

Fig. 13. Identifying critical parameters for the evaluation of ML models in Al/FTO/In_2S_3/Be_3SbF_3/Cu_2O/Ni SCs.

affinity, temperature, and bulk defect density exert relatively negligible effects under typical conditions. The research indicates that optimizing the bandgap and reducing interface defects are the most effective methods for enhancing perovskite solar cell performance.

An exhaustive evaluation of the model's performance

The performance of the model was meticulously assessed using a range of statistical indicators, as detailed in Table 6, to guarantee the accuracy and generalizability of the RF predictions. The R^2 values indicated a significant correlation between predicted and experimental results, attaining 0.9894 for V_{OC}, 0.9881 for PCE, 0.9892 for J_{SC}, and 0.9814 for FF. The results demonstrate the model's capacity to accurately represent complex physical dependencies and nonlinear connections among PV parameters. Moreover, the reduced values recorded for Mean Squared Error (MSE), Root Mean Squared Error (RMSE), Mean Absolute Error (MAE), and Mean Absolute Percentage Error (MAPE) corroborate the model's stability and minimum divergence from experimental standards. These indications collectively yield an overall prediction accuracy of 98.7%, highlighting the robustness and trustworthiness of the RF method in correlating material attributes with device performance results. The feature selection process was crucial in improving the model's interpretability and computational efficiency by methodically eliminating redundant or weakly correlated variables. This enhancement maintained the model's predictive ability while expediting training convergence and augmenting generalization to novel data. Fig. S3a–d illustrates a nearly perfect correlation between the projected and actual data points along the ideal $y = x$ line, affirming the model's robust consistency and minimal prediction bias. These findings confirm the RF approach as a robust and interpretable machine learning framework for quantitative prediction, sensitivity analysis, and design optimization of PSCs. Its capacity to amalgamate several performance indicators while preserving precision and stability establishes RF as a highly dependable method for directing the future development of high-efficiency, lead-free perovskite devices.

Analysis of correlation heatmap

Figure 14 displays a correlation heatmap that illustrates the linear correlations among several design parameters and the PCE of the PSC. Correlation coefficients between −1 and +1 signify the strength and direction of relationships, with positive values denoting direct associations and negative values representing inverse trends. The analysis indicates that absorber thickness demonstrates a modest positive association with PCE ($r = 0.25$), implying that increased absorber thickness somewhat improves device performance. In contrast, bandgap energy exhibits a significant negative correlation ($r = -0.65$), indicating that bigger bandgaps diminish efficiency. Parameters like acceptor density ($r = -0.16$) and defect density ($r = -0.11$) exhibit weak negative associations, suggesting that excessive doping or structural imperfections marginally impair performance. Likewise, interface imperfections exhibit a moderate negative correlation ($r = -0.36$), substantiating their adverse impact on charge transport and overall efficiency.

Additional parameters such as electron affinity, dielectric permittivity, electron mobility, hole mobility, and temperature demonstrate weak or negligible correlations, indicating minimal direct impact on PCE. The heatmap indicates that bandgap energy and absorber thickness are the primary factors affecting device efficiency. The relatively weak correlations among most variables highlight their relative independence, hence validating the application of nonlinear machine learning models such as Random Forest to elucidate the intricate interdependencies influencing solar cell performance.

SHAP-based importance analysis for comprehending feature contributions

Figure 15 presents the SHAP (Shapley Additive Explanations) summary graphic, which delineates the contribution of each design parameter to PCE as predicted by the Random Forest model. SHAP values on the x-axis measure the impact of each feature positive values denote an enhancement in PCE, whilst negative values suggest a decline in performance. The research finds bandgap energy and interface defect density as the most significant detrimental factors, demonstrating that elevated values of both parameters substantially decrease PCE.

These data align with the correlation heatmap, validating their significant detrimental effect on charge transport and recombination. Defect density exerts a slight negative impact, underscoring the necessity of reducing structural flaws. Conversely, absorber thickness exhibits a significant positive SHAP effect, indicating that an increase in thickness enhances light absorption and device efficiency. Electron mobility has a minor positive contribution, whereas temperature, electron affinity, acceptor density, hole mobility, and dielectric permittivity show minimal impact, with SHAP values around zero. The SHAP analysis identifies bandgap energy and interface defect density as primary factors limiting efficiency, whereas absorber thickness and carrier

Parameter	MSE	RMSE	MAE	R^2	MAPE
V_{OC}	0.0012	0.0022	0.0011	0.9894	0.06%
J_{SC}	0.0016	0.0245	0.0084	0.9892	0.08%
FF	0.0057	0.0755	0.0224	0.9814	0.02%
PCE	0.0037	0.0606	0.0235	0.9881	0.14%
Average	0.00305	0.0407	0.01385	0.987	0.075

Table 6. Evaluating forecast accuracy for key PV parameters through various types of measures.

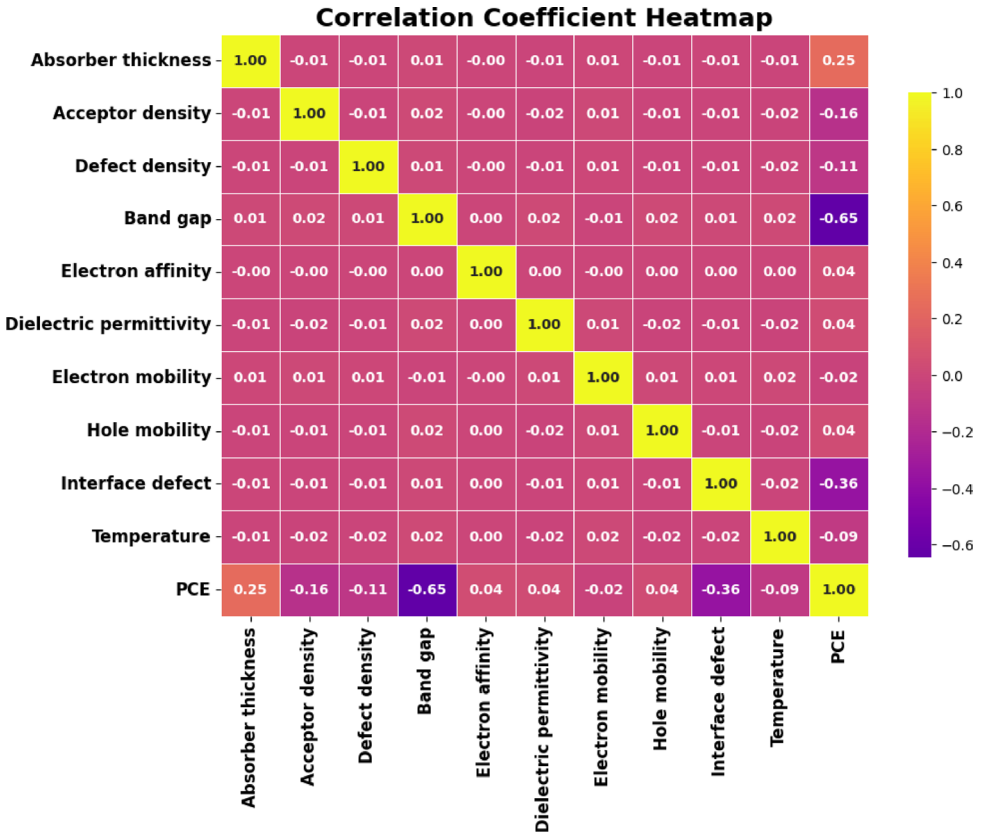

Fig. 14. Utilizing a correlation heatmap to illustrate the interactions between factors in the proposed SC configuration.

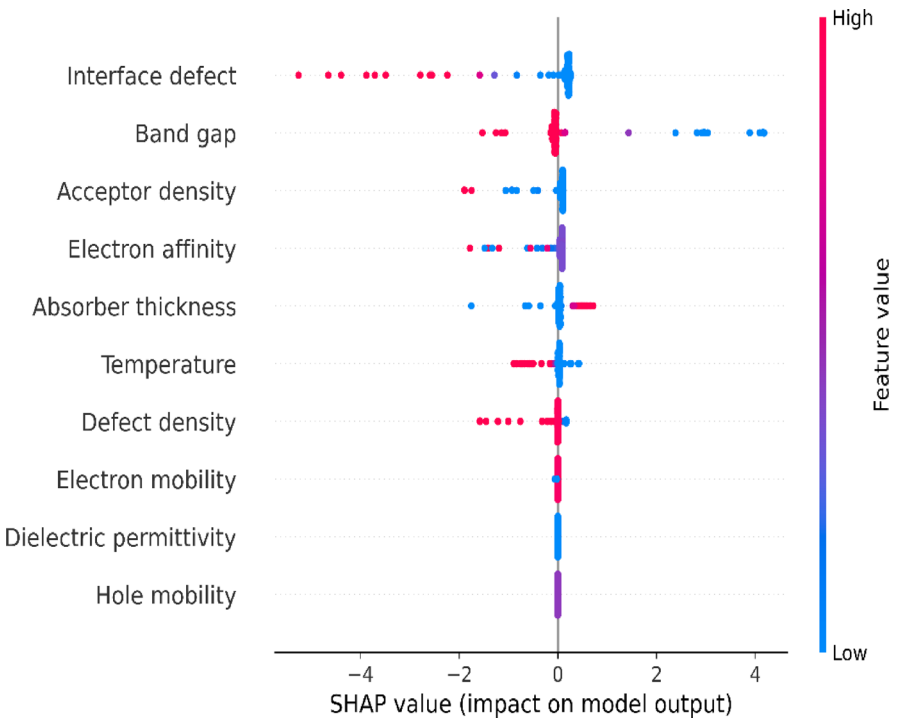

Fig. 15. Thorough examination of variable influences on PCE using SHAP values, with rankings determined by their significance in the rf regression model.

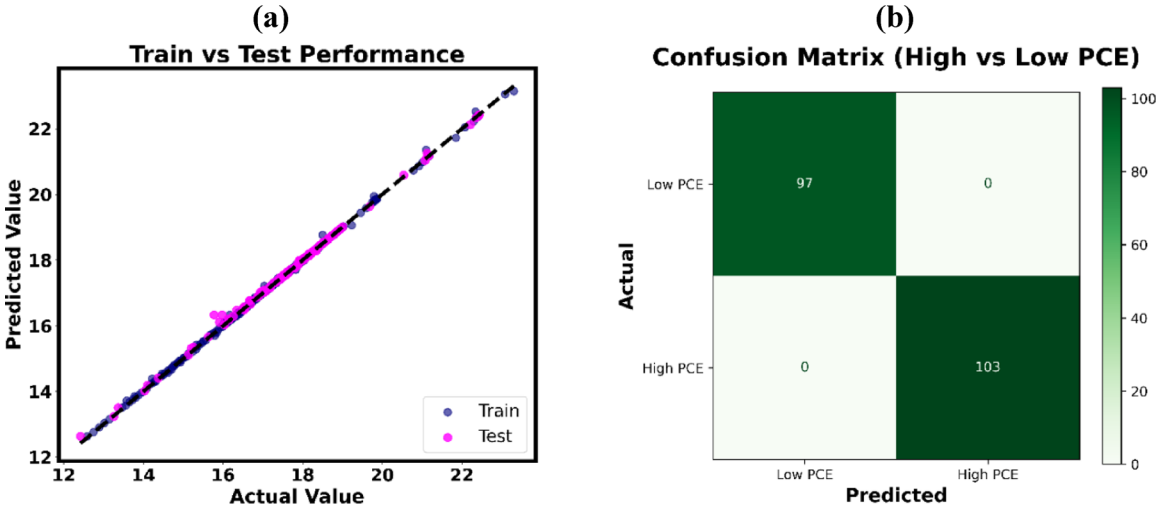

Fig. 16. Performance evaluation of the proposed solar cell design as demonstrated by (**a**) parity plot and (**b**) confusion matrix.

mobility serve as secondary enhancers. These insights offer essential recommendations for enhancing PSC architecture and attaining superior performance.

Evaluating model performance through parity plot and confusion matrix
The predictive efficacy of RF model was assessed by regression and classification studies, yielding a thorough comprehension of its correctness in modeling PSCs. Figure 16a illustrates that the scatter plot predicted against actual values for both the training and testing datasets demonstrates a robust correlation along the diagonal line, signifying exceptional concordance with experimental data. The substantial overlap between training (blue) and testing (magenta) points validates the model's superior prediction accuracy and strong generalization to novel data, effectively reducing overfitting. The results underscore the RF model's capability in identifying nonlinear relationships among essential PV parameters, including bandgap, defect density, and carrier mobility.

Figure 16b presents a confusion matrix that further corroborates the model's classification efficacy in differentiating between high- and low-efficiency PSCs. The matrix demonstrates flawless classification accuracy, comprising 97 true negatives (Low PCE) and 103 genuine positives (High PCE), with no erroneous predictions. This illustrates the model's dependability in accurately categorizing device efficiency levels without error. The regression and classification outcomes collectively validate that the RF model can properly forecast PV performance and effectively distinguish across device quality categories. This dual predictive capability enhances data-driven decision-making in material selection, structural design, and process optimization. The results highlight the revolutionary impact of machine learning in PV research, facilitating the methodical and intelligent design of next-generation PSCs with improved efficiency and stability.

Feasibility of device fabrication

To actualize the computationally predicted performance, the fabrication feasibility of Be_3SbF_3-based perovskite solar cells (PSCs) necessitates a meticulously organized experimental framework that includes material synthesis, device assembly, stability assessment, advanced characterization, and strategies for efficiency enhancement. This methodical methodology not only corroborates theoretical conclusions but also establishes a solid basis for enhancing performance in practical scenarios.

- **Synthesis and preparation of materials**

1. *Synthesis of Be_3SbF_3*: High-purity Be_3SbF_3 can be produced using solid-state reaction, chemical vapor deposition (CVD), or solution-based processes, contingent upon the required film thickness and scalability. Maintaining stoichiometric accuracy and phase consistency is essential, as these elements directly affect charge transfer and optical absorption efficiency.
2. *Structural and morphological characterization*: X-ray diffraction (XRD) will ascertain crystal structure and phase purity, while scanning electron microscopy (SEM) and transmission electron microscopy (TEM) will offer comprehensive insights into surface morphology, grain connectivity, and defect density.
3. *Compositional engineering and doping*: Strategic doping and alloying techniques can be employed to precisely adjust electrical conductivity and enhance stability. Inductively coupled plasma mass spectrometry (ICP-MS) and energy-dispersive X-ray spectroscopy (EDS) guarantee compositional uniformity and identify trace contaminants.

- **Fabrication of devices**

1. *Solar cell construction*: Layer deposition can be accomplished using spin coating, thermal evaporation, or sputtering, resulting in a planar heterojunction device structure, exemplified by Al/FTO/In_2S_3/Be_3SbF_3/Cu_2O/Ni. To avert deterioration from oxygen and moisture, manufacture must take place within an inert environment glovebox.
2. *Quality control*: The uniformity of layer production and the accuracy of thickness control can be assessed by atomic force microscopy (AFM) and profilometry. Elevated interfacial uniformity guarantees efficient charge extraction and reduces recombination losses.

- **Optimization of efficiency using optical engineering**

Considering that Be_3SbF_3 possesses a moderate indirect bandgap, the use of anti-reflective coatings (ARCs) can markedly improve light absorption, especially in the ultraviolet (UV) and visible spectrum regions where reflectivity losses are substantial. Materials like MgF_2, SiO_2, Si_3N_4, or TiO_2 nanolayers can serve as anti-reflective coatings to diminish surface reflection, enhance photon absorption, and elevate overall PCE[104]. Additionally, textured transparent conducting oxides (TCOs) or graded refractive index coatings may be investigated to prolong optical path lengths and improve light trapping within the absorber layer. The integration of ARCs is particularly advantageous for low-absorption materials, as it efficiently mitigates the constraints of optical thickness without elevating recombination concerns.

- **Assessment of stability**

1. *Environmental stability*: Devices must undergo humidity and oxygen exposure assessments, along with regular J-V measurements to evaluate degradation kinetics. Accelerated aging experiments under constant illumination and elevated temperature circumstances can replicate long-term operating stability.
2. *Thermal and mechanical stability*: Thermal cycling and mechanical bending assessments are crucial for evaluating the durability of flexible or temperature-sensitive setups. These results confirm that Be_3SbF_3 preserves both structural integrity and efficiency under varying operational settings.

- **Comparative and benchmarking evaluation**

1. *Reference cells*: Performance benchmarks should be established by fabricating reference solar cells utilizing silicon and lead-based perovskites under identical conditions. A comparative assessment of J_{SC}, V_{OC}, FF, and PCE yields essential insights into the competitiveness of Be_3SbF_3 absorbers.
2. *Simulation correlation*: Experimental results must be juxtaposed with SCAPS-1D simulation data, emphasizing critical parameters such carrier lifespan, recombination rate, and defect density. Discrepancies between experimental and simulated data will inform iterative enhancements in both modeling and manufacturing processes.

- **Sophisticated characterization methods**

1. *Interface and defect analysis*: Interfaces and defect states can be examined by X-ray photoelectron spectroscopy (XPS) and Fourier-transform infrared spectroscopy (FTIR) to evaluate chemical bonding and energy-level alignment. Deep-level transient spectroscopy (DLTS) can provide additional quantification of trap states and charge carrier dynamics.
2. *Microscopic and electrical mapping*: Techniques such as Kelvin probe force microscopy (KPFM) and conductive atomic force microscopy (c-AFM) provide the imaging of localized potential changes and charge transport dynamics at the nanoscale, providing enhanced understanding of interfacial quality and electronic uniformity.

- **Scalability and market potential**

Commercializing Be_3SbF_3-based solar cells necessitates addressing problems pertaining to stability, scalable production, interface optimization, and cost efficiency. Utilizing encapsulation methods and moisture barriers can enhance environmental resistance. Concurrently, solution-processable large-area deposition techniques, like slot-die coating and blade coating, might enhance industrial scalability. Moreover, including ARCs in large-scale production could significantly enhance module efficiency without modifying absorber chemistry. Alongside economical synthesis and robust interfacial engineering, these advancements establish Be_3SbF_3 as a feasible lead-free option for next-generation, high-performance optoelectronic and photovoltaic devices. This comprehensive method connects theoretical modeling with practical verification, thereby progressing the development of commercially viable Be_3SbF_3 perovskite solar systems.

Conclusion

This study conducts a thorough examination of the structural, optoelectronic, and PV characteristics of Be_3MF_3 (M = P, As, Sb) perovskites utilizing an integrated methodology that merges DFT with SCAPS-1D simulations. First-principles of DFT computations were utilized to investigate the structural stability, electronic band structure, charge transport, and optical characteristics of these materials. All compounds demonstrated a persistent cubic phase, in accordance with theoretical predictions, and an indirect semiconducting band structure. Optical study demonstrated a wide absorption spectrum and a tight band gap, designating Be_3SbF_3 as a viable solar absorber with significant light-harvesting capability. Photovoltaic simulations utilizing Be_3SbF_3 as the absorber across four device designs revealed that the Al/FTO/In_2S_3/Be_3SbF_3/Cu_2O/Ni configuration attained exceptional

performance, with V_{OC} of 1.79 V, J_{SC} of 11.04 mA/cm^2, FF of 89.6%, and PCE of 18.28%. The improved performance is due to advantageous band alignment, effective charge extraction, and minimal interfacial recombination. The influence of absorber and ETL thickness, defect density, acceptor density, and temperature was examined, indicating best efficiency at an absorber thickness of 1 µm, although increased temperature diminished V_{OC}, FF, and PCE. Further assessments of QE and J-V characteristics enhanced understanding of device functionality. The RF machine learning model was employed to enhance performance utilizing SCAPS-1D data. connection heatmap and SHAP studies revealed that bandgap energy and interface defect density are significant negative determinants of PCE, but absorber thickness exhibited a positive connection. The parity plot demonstrated exceptional prediction accuracy ($R^2 = 0.987$), while the confusion matrix attained classification accuracy. These findings collectively establish a data-driven paradigm for the design and optimization of Be_3MF_3-based PSCs, providing vital insights for next-generation, high-efficiency PV systems.

Data availability

Data will be made available on request.

Received: 27 October 2025; Accepted: 23 December 2025
Published online: 08 January 2026

References

1. Ukoba, K., Yoro, K. O., Eterigho-Ikelegbe, O., Ibegbulam, C. & Jen, T.-C. Adaptation of solar energy in the global South: Prospects, challenges and opportunities. *Heliyon* **10**, e28009 (2024).
2. Ashraf, A. & Sagheer, M. Renewable energy capacity and technological innovations: A review of global trends and future directions. *Environ. Prog. Sustain. Energy* https://doi.org/10.1002/ep.70071 (2025).
3. Jamesh, M.-I. et al. Advancement of technology towards developing perovskite-based solar cells for renewable energy harvesting and energy transformation applications. *Npj Mater. Sustain.* **3**, 29 (2025).
4. Shah, A. U. I. & Meyer, E. L. Perovskite-based solar cells in photovoltaics for commercial scalability: Current progress, challenges, mitigations and future prospectus. *Sol. Energy* **286**, 113172 (2025).
5. Islam, S. et al. Introducing a new and highly efficient double-absorber solar cell with combination of Sr_3 PBr_3 and $CsPbI_3$ Perovskites. *Phys. Status Solidi A* **222**, 2500148 (2025).
6. Hooda, N., Kundara, R., Chaudhary, S. & Baghel, S. Numerical modelling of lead-free $AgZnF_3$ perovskite solar cells with over 31% efficiency: A SCAPS-1D investigation. *Phys. Scr.* **100**, 105961 (2025).
7. Hong, S. Y., Lee, D. S., Lee, H. J., Hong, K.-H. & Im, S. H. Recent progress in Pb-, Sn-, and Pb–Sn-based inorganic perovskite solar cells: Toward enhanced stability and efficiency. *EES Sol.* **1**, 441–481 (2025).
8. Lu, X. et al. Ecotoxicity and sustainability of emerging Pb-based photovoltaics. *Sol. RRL* **6**, 2200699 (2022).
9. Kishor, A. et al. Performance enhancement of carbon-based solar cells using SWCNT absorber: A SCAPS-1D simulation and DFT study. *Phys. Scr.* **100**, 095526 (2025).
10. Kim, B. et al. Improved stability of $MAPbI_3$ perovskite solar cells using two-dimensional transition-metal dichalcogenide interlayers. *ACS Appl. Mater. Interfaces* **14**, 35726–35733 (2022).
11. Raj, M., Aggarwal, A., Kushwaha, A. & Goel, N. Optimization of Cs_2 $SnBr_6/C_s2$ Te_16 bilayer absorber for enhanced performance in perovskite solar cell. *Phys. Scr.* **100**, 116007 (2025).
12. Parmar, V. B., Gajjar, P. N. & Vora, A. M. Investigation of the efficiency of non-toxic $RbGeX_3$ (X = I, Br, Cl) perovskites as absorption layer in solar energy converters based on thickness dependency. *Phys. Scr.* **100**, 065975 (2025).
13. Ur Rehman, J. et al. First-principles calculations to investigate structural, electronics, optical and elastic properties of Sn-based inorganic Halide-perovskites CsSnX3 (X = I, Br, Cl) for solar cell applications. *Comput. Theor. Chem.* **1209**, 113624 (2022).
14. Zhang, S. et al. A DFT approach to explore the structural, mechanical, and optoelectronic of indium-based InXY3 (X = Ca, Sr, Ba; Y = Cl, Br) halide perovskites for photoelectric applications. *Phys. Lett. A* **533**, 130243 (2025).
15. Rahman, M., Lubaba, A., Irfan, A. & Rahman, Md. F. New double perovskite solar cell containing Ba_3 PCl_3 (A_3 BX_3) and $CsSnI_3$ (ABX_3) leading to an improved efficiency above 30%. *ChemistrySelect* **9**, e202403217 (2024).
16. Apurba, I. K. G. G., Islam, Md. R., Rahman, Md. S., Rahman, Md. F. & Ahmad, S. Exploring the inorganic perovskite materials Mg_3SbX_3 (Where, X=I, Br, Cl and F) through the perspective of density functional theory: Adjustment of physical characteristics as consequence of strain. *Heliyon* **10**, e39218 (2024).
17. Islam, Md. A. I., Rahman, Md. F., Islam, Md. M., Mohammed, M. K. A. & Irfan, A. Investigation of novel all-inorganic perovskites Ba_3 PX_3 (X = F, Cl, Br, I) with efficiency above 29%. *Phys. Chem. Chem. Phys.* **27**, 1861–1883 (2025).
18. Ghosh, A. et al. Examining the electronic, structural, optical, and photovoltaic capabilities of Sr3AsBr3 perovskite under tensile and compressive strains with DFT and SCAPS-1D. *Surf. Interfaces* **54**, 105195 (2024).
19. Harun-Or-Rashid, Md. et al. Analysis of the role of A-cations in lead-free A3SbI3 (A = Ba, Sr, Ca) perovskite solar cells. *J. Mater. Sci.* **59**, 6365–6385 (2024).
20. Hossain, A. et al. A first-principles study on structural, electronic, optical and thermal characteristics of A_3 BF_3 (A = Mg, Ca, Sr, Ba; B = N, Bi) perovskites towards multifunctional applications. *Phys. Scr.* **100**, 0759b1 (2025).
21. Ghosh, A. et al. Investigating of novel inorganic cubic perovskites of A3BX3 (A=Ca, Sr, B P, As, X=I, Br) and their photovoltaic performance with efficiency over 28%. *J. Alloys Compd.* **986**, 174097 (2024).
22. Zhao, R. et al. Wide bandgap tuning of violet phosphorus quantum dots by functionalization. *J. Phys. Chem. Lett.* **13**, 8236–8244 (2022).
23. Zhong, M. et al. Thickness-dependent carrier transport characteristics of a new 2D elemental semiconductor: Black arsenic. *Adv. Funct. Mater.* **28**, 1802581 (2018).
24. Li, J. et al. Antimony contamination, consequences and removal techniques: A review. *Ecotoxicol. Environ. Saf.* **156**, 125–134 (2018).
25. Caron, S. Where does the fluorine come from? A review on the challenges associated with the synthesis of organofluorine compounds. *Org. Process. Res. Dev.* **24**, 470–480 (2020).
26. Gao, S., Luo, Y., Liu, X. & Marom, N. Predicting the excited-state properties of crystalline organic semiconductors using GW+BSE and machine learning. *Digit. Discov.* **4**, 1306–1322 (2025).
27. Boutramine, A. et al. Insights into the thermodynamic, optoelectronic, and thermoelectric properties of ternary transition metal chalcogenides BiIrQ (Q = S, Se, Te) for next-generation optoelectronic and energy harvesting technologies: A DFT and AIMD study. *Surf. Interfaces* **72**, 107269 (2025).
28. Rabhi, S. et al. Insight into NaSiCl3: A lead-free perovskite for the next generation revealed by DFT and SCAPS-1D. *Phys. Chem. Chem. Phys.* **27**, 13490–13507 (2025).
29. Khan, A. N. et al. Evaluating A2SrGeI6 (A = K and Rb) lead-free double perovskites: Structural, elastic, and optoelectronic insights for clean energy. *Inorg. Chem. Commun.* **174**, 113949 (2025).

30. Haque, M. M., Shimul, A. I., Ghosh, A., Awwad, N. S. & Chaudhry, A. R. Investigation of pressure-driven band gap variation and the physical characteristics of Ba_3 SbX_3 (X = F, Cl) perovskite for potential optoelectronic applications. *Opt. Express* **33**, 30486 (2025).
31. Burgelman, M., Decock, K., Khelifi, S. & Abass, A. Advanced electrical simulation of thin film solar cells. *Thin Solid Films* **535**, 296–301 (2013).
32. Hafaifa, L. et al. High-efficiency CGS/CZTSSe tandem thin-film solar cells: A simulation-based study. *Phys. Scr.* **100**, 095949 (2025).
33. Bouri, N. et al. Resistance dynamics in a solar cell with novel lead-free perovskite absorbers (LiMgI3 and NaMgI3): Performance optimization using SCAPS-1D simulation and impedance spectroscopy. *J. Phys. Chem. Solids* **207**, 112972 (2025).
34. Elhadi, M. et al. Optimization and comparative analysis of electron transport layers for high-performance $InGeCl_3$ -Based perovskite solar cells. *ChemistrySelect* **10**, e01364 (2025).
35. Rahman, Md. F. et al. The impact of group V cation substitution on the structural and functional properties of Sr3MF3 (M = Sb, As, P, N) fluoro-perovskites. *Inorg. Chem. Commun.* **182**, 115426 (2025).
36. Harun-Or-Rashid, Md. et al. Revealing $InPbBr_3$ perovskite's potential: A DFT, scaps and machine learning-based study for next-generation solar cells. *NANO* https://doi.org/10.1142/S1793292026500037 (2025).
37. Rahman, Md. F. et al. Achieving efficiency above 30% with new inorganic cubic perovskites X_2 $SnBr_6$ (X = Cs, Rb, K, Na) *via* DFT and SCAPS-1D. *Phys. Chem. Chem. Phys.* **27**, 1155–1170 (2025).
38. Hasan, Md. M. et al. Control of B-cation and X-anion atoms in inorganic Pb-free novel Mg_3 BX_3 (B = P, N; X = Br, I) perovskites: A first-principles framework. *New J. Chem.* **49**, 6298–6312 (2025).
39. Talukder, M. R. et al. Theoretical insights into novel Ba3MX3 (M = P, Sb; X = F, Cl) perovskites for advanced optoelectronics: A first-principles DFT study. *Comput. Theor. Chem.* **1248**, 115239 (2025).
40. Mishra, K. K., Chahar, S. & Sharma, R. An extensive investigation of structural, electronic, and optical properties of inorganic perovskite Ca3AsCl3 for photovoltaic and optoelectronic applications: A first-principles approach using quantum ATK tool. *Solid State Commun.* **390**, 115623 (2024).
41. Hernández-Haro, N., Ortega-Castro, J., Martynov, Y. B., Nazmitdinov, R. G. & Frontera, A. DFT prediction of band gap in organic-inorganic metal halide perovskites: An exchange-correlation functional benchmark study. *Chem. Phys.* **516**, 225–231 (2019).
42. Rehman, M. A. et al. Study of physical properties of Cs2TlGaX6 (X = Cl, Br) halide perovskites via HSE-06 hybrid technique for high efficiency solar cells. *Opt. Quantum Electron.* **56**, 1079 (2024).
43. Datta, A. K. et al. DFT insights into bandgap engineering of lead-free LiMCl3 (M = Mg, Be) halide perovskites for optoelectronic device applications. *Sci. Rep.* **15**, 6944 (2025).
44. Dutta, R. et al. Optical enhancement of indirect bandgap 2D transition metal dichalcogenides for multi-functional optoelectronic sensors. *Adv. Mater.* **35**, 2303272 (2023).
45. Jang, W. J., Jang, H. W. & Kim, S. Y. Recent advances in wide bandgap perovskite solar cells: Focus on lead-free materials for tandem structures. *Small Methods* **8**, 2300207 (2024).
46. Nashia, T. S. et al. Computational investigation of LiMgZ half-heusler phases where Z = P, as, and Bi for optoelectronic and photoelectronic applications. *Sci. Rep.* **15**, 33943 (2025).
47. Parves, Md. S. et al. Optimized solar conversion achieved with double halide X2NaIrCl6 (X = Rb, Cs) perovskites for optoelectronic and photovoltaic applications. *Energy Nexus* **20**, 100549 (2025).
48. He, R. et al. Wide-bandgap organic–inorganic hybrid and all-inorganic perovskite solar cells and their application in all-perovskite tandem solar cells. *Energy Environ. Sci.* **14**, 5723–5759 (2021).
49. Bakkar Siddique, Md. A. et al. Exploring optoelectronic behavior and solar cell efficiency of double halide perovskites M_2 $KIrCl_6$ (M = Cs, Rb) through DFT and SCAPS-1D. *Langmuir* **41**, 19797–19820 (2025).
50. Khan, M. I. et al. Impact of Cr doping on the structural and optoelectronic properties of a $CsPbIBr_2$ perovskite solar cell. *New J. Chem.* **48**, 7205–7212 (2024).
51. Shimul, A. I., Chandra Biswas, B., Ghosh, A., Alrafai, H. A. & Hassan, A. A. A study on optoelectronic properties and charge transport layer influence in novel Sr3PF3-Based perovskite solar cells using numerical simulation and machine learning. *Sol. Energy Mater. Sol. Cells* **293**, 113838 (2025).
52. Aziz, F., Khalid, S., Fatima, R., Ahmed, M. & Ali, H. E. A DFT study to explore structural, elastic, mechanical, electronic and optical properties of inverse perovskite SbPMg3 for solar cell applications. *Mater. Sci. Semicond. Process.* **184**, 108755 (2024).
53. Mirza, S. H., Malik, N. H., Yousuf, M. W., Knani, S. & Parveen, A. Investigating the effect of hydrostatic pressure on the essential physical properties of cubic $SrTiO_3$ perovskite for cost-effective energy solutions and solar cell advancement: A density functional theory and SCAPS-1D study. *Energy Technol.* https://doi.org/10.1002/ente.202500061 (2025).
54. Khan, J. et al. First-principles study on the structural, optoelectronic, and elastic properties of halide perovskites $XSnCl_3$ (X = Rb, Cs) for photoelectrode applications. *J. Inorg. Organomet. Polym. Mater.* **35**, 4162–4175 (2025).
55. Hosen, A. Investigating the effects of hydrostatic pressure on the physical properties of cubic Sr3BCl3 (B = As, Sb) for improved optoelectronic applications: A DFT study. *Heliyon* **10**, e35855 (2024).
56. Hasan, N., Arifuzzaman, M. & Kabir, A. Structural, elastic and optoelectronic properties of inorganic cubic $FrBX_3$ (B = Ge, Sn; X = Cl, Br, I) perovskite: the density functional theory approach. *RSC Adv.* **12**, 7961–7972 (2022).
57. Zhang, M., Li, Z., Gong, Z., Li, Z. & Zhang, C. Perspectives on the mechanical robustness of flexible perovskite solar cells. *Energy Adv.* **2**, 355–364 (2023).
58. Park, N.-G. & Zhu, K. Scalable fabrication and coating methods for perovskite solar cells and solar modules. *Nat. Rev. Mater.* **5**, 333–350 (2020).
59. Liu, R. et al. Band alignment engineering in two-dimensional transition metal dichalcogenide-based heterostructures for photodetectors. *Small Struct.* **2**, 2000136 (2021).
60. Latif, H. et al. Effect of target morphology on morphological, optical and electrical properties of FTO thin film deposited by pulsed laser deposition for $MAPbBr_3$ perovskite solar cell. *Surf. Interfaces* **24**, 101117 (2021).
61. Hashemi, M. et al. Electrical and optical characterization of sprayed In2S3 thin films as an electron transporting layer in high efficient perovskite solar cells. *Sol. Energy* **215**, 356–366 (2021).
62. Chowdhury, A., Ghosh, A., Rifat-E-Rasul, Md & Islam, Md. R. Exploring pressure-induced changes in the electronic, mechanical and optical properties of inorganic Sr_3 AsI_3 perovskite. In *2024 13th International Conference on Electrical and Computer Engineering (ICECE)* 218–223 (IEEE, Dhaka, Bangladesh, 2024). https://doi.org/10.1109/ICECE64886.2024.11024763.
63. Paul, I., Rayhan, A. & Khan, M. A. Design and performance analysis of photovoltaic solar cells using WSe2 as an absorber layer with SnS2 electron transport layer. *New Energy Exploit. Appl.* **4**, 83–101 (2025).
64. Ahmmed, S., Aktar, A. & Ismail, A. BMd. Role of a solution-processed V_2 O_5 hole extracting layer on the performance of CuO-ZnO-based solar cells. *ACS Omega* **6**, 12631–12639 (2021).
65. Ferhati, H., AbdelMalek, F. & Djeffal, F. Improved PCE in stable lead-free perovskite solar cells based on band engineering of ETL and absorber. *Sol. Energy* **262**, 111805 (2023).
66. Li, H. et al. Self-enhanced antibacterial and antifouling behavior of three-dimensional porous Cu_2 O nanoparticles functionalized by an organic-inorganic hybrid matrix. *ACS Appl. Mater. Interfaces* **15**, 38808–38820 (2023).
67. Kacor, P., Bernat, P., Mlcak, T. & Hrabovsky, L. Realization of a test tool for diagnosis of contact resistance and measurement of selected types of conductive materials. *Sensors* **23**, 5867 (2023).

68. Da, S., Liu, W., Li, C., Lei, Y. & Ran, F. Regulation of interface schottky barrier and photoelectric properties in carbon-based HTL-free perovskite solar cells. *Small* **21**, 2408923 (2025).
69. Ishraq, M. H. et al. ETL and HTL engineering in CH_3 NH_3 $PbBr_3$ perovskite for stable and efficient performance photovoltaic devices applications using SCAPS- 1D. *Adv. Theory Simul.* **7**, 2400360 (2024).
70. Ma, X., Janssen, R. A. J. & Gelinck, G. H. Trap-assisted charge generation and recombination in State-of-the-Art organic photodetectors. *Adv. Mater. Technol.* **8**, 2300234 (2023).
71. Asif, P., Chetia, A., Saikia, D. & Sahu, S. A comprehensive theoretical investigation of lead-free mixed antimony-bismuth halide double perovskite ($Cs_2AgBi_{0.75}Sb_{0.25}Br_6$) solar cell using SCAPS-1D. *Discov. Electron.* **2**, 44 (2025).
72. Islam, Md. S. et al. Machine learning approach to delineate the impact of material properties on solar cell device physics. *ACS Omega* **7**, 22263–22278 (2022).
73. Reza, M., Ghosh, A., Reza, M., Wornob, S. N. & Sultana, S. Design and efficiency improvement of eco-conscious Sr3PBr 3 and Sr3NCl3 double perovskite solar cells with IGZO and Cu2O as ETL and HTL. *Energy Nexus* **18**, 100417 (2025).
74. Boujelbene, M. et al. Achieving 34 % efficiency with a dual-absorber solar cell design using CaRbCl3 and Ca3NCl3 perovskites. *Inorg. Chem. Commun.* **170**, 113472 (2024).
75. Afonso, D., Mesbahi, O., Bouich, A. & Tlemçani, M. Influence of long-term and short-term solar radiation and temperature exposure on the material properties and performance of photovoltaic panels: A comprehensive review. *Energies* **18**, 5072 (2025).
76. Mottakin, M. et al. Design and modelling of eco-friendly ch3nh3sni3-based perovskite solar cells with suitable transport layers. *Energies* **14**, 7200 (2021).
77. Wang, Z. et al. Toward high efficient Cu_2 $ZnSn(S_x, Se_{1-x})_4$ solar cells: Break the limitations of V_{OC} and FF. *Small* **19**, 2300634 (2023).
78. Sani, S. et al. A study on defect, doping, and performance of ETLs (ZnO, TiO_2, and IGZO) for the lead-free $CsSnCl_3$ perovskite solar cell by SCAPS-1D framework. *Mater. Today Commun.* **38**, 107575 (2024).
79. Von Hauff, E. & Klotz, D. Impedance spectroscopy for perovskite solar cells: characterisation, analysis, and diagnosis. *J. Mater. Chem. C* **10**, 742–761 (2022).
80. Guerrero, A., Bisquert, J. & Garcia-Belmonte, G. Impedance spectroscopy of metal halide perovskite solar cells from the perspective of equivalent circuits. *Chem. Rev.* **121**, 14430–14484 (2021).
81. Aliaghayee, M. Optimization of the perovskite solar cell design with layer thickness engineering for improving the photovoltaic response using SCAPS-1D. *J. Electron. Mater.* **52**, 2475–2491 (2023).
82. Yuan, J., Ai, Z., Yu, M., Huang, R. & Cheng, Q. Growth and application of $MoSe_2$ in solar cells. *Int. J. Mod. Phys. B* **36**, 2250168 (2022).
83. Zhou, Y. et al. Solution-processed antimony selenide heterojunction solar cells. *Adv. Energy Mater.* **4**, 1301846 (2014).
84. Liu, X. et al. Enhanced open circuit voltage of Sb2Se3/CdS solar cells by annealing Se-rich amorphous Sb2Se3 films prepared via sputtering process. *Sol. Energy* **195**, 697–702 (2020).
85. Bulowski, W. et al. Optimization of the ETL titanium dioxide layer for inorganic perovskite solar cells. *J. Mater. Sci.* **59**, 7283–7298 (2024).
86. Li, F. et al. Perovskite quantum Dot Solar Cells with 15.6% efficiency and improved stability enabled by an α-CsPbI3 /FAPbI3 bilayer structure. *ACS Energy Lett.* **4**, 2571–2578 (2019).
87. Zhao, Q. et al. High efficiency perovskite quantum dot solar cells with charge separating heterostructure. *Nat. Commun.* **10**, 2842 (2019).
88. Shimul, A. I., Hossain, M. M. & Dipa, S. A. Investigating the effectiveness of Ca3AsCl3-based Perovskite Solar Cells with optimal hole transport layer selection through numerical optimization and machine learning. *Opt. Commun.* **586**, 131916 (2025).
89. Ahmad, W., Noman, M., Tariq Jan, S. & Khan, A. D. Performance analysis and optimization of inverted inorganic $CsGeI_3$ perovskite cells with carbon/copper charge transport materials using SCAPS-1D. *R. Soc. Open Sci.* **10**, 221127 (2023).
90. Raj, M., Aggarwal, A., Kushwaha, A. & Goel, N. Exploring $RbGeI_3$ based perovskite solar cells: a comprehensive DFT study and SCAPS analysis with copper-based hole transport layers. *Opt. Quantum Electron.* **57**, 435 (2025).
91. Aggarwal, A., Raj, M., Narayan, A., Kushwaha, A. & Goel, N. Machine learning-guided design of Cs_2 $SnBr_6$ -based solar cells: A DFT and SCAPS-1D analysis with N-doped Ti_O2 HTL. *Phys. Scr.* **100**, 085946 (2025).
92. Raj, M., Aggarwal, A., Kushwaha, A. & Goel, N. Moisture-resistant sustainable solar cell with RbGeI3 absorber layer. *J. Mater. Sci.* **60**, 9176–9196 (2025).
93. Rahman, Md. A. et al. Impact of A-Cations modified on the structural, electronic, optical, mechanical, and solar cell performance of inorganic novel A_3 NCl_3 (A = Ba, Sr, and Ca) perovskites. *Energy Fuels* **38**, 8199–8217 (2024).
94. Elboughdiri, N. et al. Innovative computational framework for Sr_3 $SbCl_3$ absorber optimization: DFT, SCAPS-1D, and machine learning perspectives. *New J. Chem.* **49**, 14529–14552 (2025).
95. Reza, Md. S. et al. Tuning the hole transport layer in the Ca3SbI3 absorber-based solar cells to improve the power conversion efficiency. *J. Phys. Chem. Solids* **194**, 112250 (2024).
96. Reza, Md. S. et al. Improving the efficiency of a new perovskite solar cell based on Sr_3 SbI_3 by optimizing the hole transport layer. *Energy Fuels* **38**, 2327–2342 (2024).
97. Shrivastav, N., Madan, J. & Pandey, R. Predicting photovoltaic efficiency in Cs-based perovskite solar cells: A comprehensive study integrating SCAPS simulation and machine learning models. *Solid State Commun.* **380**, 115437 (2024).
98. Khan, T. M., Islam, B. & Ahmed, S. R. A. Performance analysis and optimization of SnSe thin-film solar cell with Cu2O HTL through a combination of SCAPS-1D and machine learning approaches. *Mater. Today Commun.* **41**, 110490 (2024).
99. Li, X., Fang, Y. & Zhao, J. Optimizing inorganic Cs4CuSb2Cl12/Cs2TiI6 dual-absorber solar cells: SCAPS-1D simulations and machine learning. *Nanomaterials* **15**, 1245 (2025).
100. Kaur, N., Pandey, R., Khalid Hossain, M. & Madan, J. Machine learning-aided optimization for transport layer parameters of low lead inorganic Zn-based mixed-halide perovskite solar cell. *Sol. Energy* **264**, 112055 (2023).
101. Ghosh, A. et al. Enhancement of sulfide-based absorber and charge transport layer solar cell performance using machine learning and the SCAPS-1D simulator. *Phys. Chem. Chem. Phys.* **27**, 15645–15668 (2025).
102. Saifee, M. A. et al. Design and performance optimization of a lead-free Cs2AgBiBr6 perovskite solar cell with graphene quantum dot hole transport layer using SCAPS-1D and machine learning. *J. Opt.* https://doi.org/10.1007/s12596-025-02539-4 (2025).
103. Asif, P., Saikia, D., Chetia, A. & Sahu, S. Comparative study of Pb-free FASnI3 based perovskite solar cells using CuI and PTAA as hole-transport materials. *Res.* **2**, 100959 (2025).
104. Thakur, A. et al. Enhancing photovoltaic parameters through anti-reflective coatings: A DFT and machine learning-based study. *J. Phys. Chem. Solids* **209**, 113320 (2026).

Acknowledgements

The researchers wish to extend their sincere gratitude to the Deanship of Scientific Research at the Islamic University of Madinah (KSA) for the support provided to the Post-Publishing Program. The authors also wish to acknowledge the developers of the SCAPS-1D software, an efficient one-dimensional solar cell simulation tool created by researchers at the Department of Electronics and Information Systems (ELIS), Ghent University, Belgium, whose contributions have been invaluable to this study.

Author contributions

Indrojit Paul, Asadul Islam Shimul, Bipul Chandra Biswas: Simulation, Formal analysis, Conceptualization, Resources, Supervision, Data curation, data acquisition, Methodology, original manuscript writing, Manuscript editing and revision, and validation. **Karim KRIAA, Mohamed Benghanem, Md. Azizur Rahman, Mekuria Tsegaye Alemu, Noureddine Elboughdiri:** Simulation, Data curation, Formal analysis, Manuscript editing and revision.

Funding

The researchers wish to extend their sincere gratitude to the Deanship of Scientific Research at the Islamic University of Madinah (KSA) for the support provided to the Post-Publishing Program.

Declarations

Competing interests

The authors declare no competing interests.

Additional information

Supplementary Information The online version contains supplementary material available at https://doi.org/10.1038/s41598-025-34000-8.

Correspondence and requests for materials should be addressed to M.T.A.